J. Fluid Mech. (2023), *vol*. 964, A24, doi:10.1017/jfm.2023.382

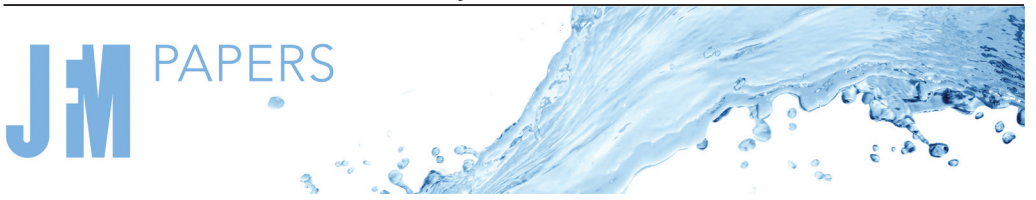

The turbulence development of a vertical natural convection boundary layer

Junhao Ke[1],†, N. Williamson[1], S.W. Armfield[1] and A. Komiya[2]

[1]School of Aerospace, Mechanical and Mechatronic Engineering, The University of Sydney, Sydney, NSW 2006, Australia

[2]Institute of Fluid Science, Tohoku University, Sendai 980-8577, Japan

(Received 23 December 2022; revised 9 March 2023; accepted 1 May 2023)

Results from direct numerical simulations of a vertical natural convection boundary layer (NCBL) with $Pr = 0.71$ reveal that the turbulence development of such a thermally driven convective flow has two distinct stages: at relatively low Grashof number, the bulk flow is turbulent while the near-wall region is laminar-like or weakly turbulent; at sufficiently high Grashof number, the entire flow becomes turbulent in the sense of von Kármán (cf. Grossmann & Lohse, *J. Fluid Mech.*, vol. 407, 2000, pp. 27–56, for the ultimate turbulent regime). Investigations on the turbulence statistics show that the near-wall Reynolds shear stress is negligible in the weakly turbulent regime but will grow in magnitude as the flow transitions to the ultimate regime at higher Grashof number. Similar behaviour is also seen in the streamwise turbulence intensity, where it develops from a mono-peak profile into a dual-peak structure as the Grashof number increases. At higher Grashof number, the near-wall energetic site is shown to have an energy distribution similar to that of a canonical wall-bounded turbulence (e.g. Hutchins & Marusic, *Phil. Trans. R. Soc.* A, vol. 365, 2007, pp. 647–664), with a peak centred at fixed location and wavelength ($y^+ = 18$ and $\lambda_x^+ = 1000$) in viscous coordinates. Investigation on the spanwise spectra also suggests that the turbulent near-wall streaks emerge only at sufficiently high Grashof number, with constant spacing $\lambda_z^+ \approx 130$. The extent of the weakly turbulent regime is identified using the maximum velocity location δ_m and a laminar length scale δ_u. The development of near-wall turbulence is also investigated by examining the turbulence kinetic energy budget. In the weakly turbulent regime, the near-wall turbulence is sustained predominantly by the pressure transport in addition to the shear production. At higher Grashof number, the flow becomes fully turbulent, and both turbulent transport and shear production become stronger, while the pressure transport is decreased. These results also reveal that the production–dissipation ratio P/ε of the NCBL

† Email address for correspondence: junhao.ke@sydney.edu.au

would follow a fundamentally different trend to the canonical wall-bounded flows, which further supports that the near-wall turbulence generation is affected by the bulk flow.

Key words: turbulent boundary layers, buoyant boundary layers, turbulent convection

1. Introduction

A vertical natural convection boundary layer (NCBL) is a fluid motion driven by buoyancy along a vertical wall when the ambient fluid temperature is different from the wall temperature. The laminar NCBL has been investigated extensively over the past several decades where the exact solutions are available (e.g. Illingworth 1950; Schetz & Eichhorn 1962). However, many industrial and geophysical NCBL flows operate beyond this thoroughly understood laminar regime at a much higher Grashof number where the flow transitions to turbulence.

Most previous literature distinguishes the onset of turbulence by examining the mean statistics and their trends with the development of the flow. In an early experimental investigation, Cheesewright (1968) reported mean statistics for a spatially developing NCBL up to $Gr_x = 10^{11}$. Here, $Gr_x = g\beta\theta_w x^3/\nu^2$ is the Grashof number based on the downstream distance x, where g is the gravitational acceleration, θ_w is the temperature difference between the isothermal wall and the ambient, β represents the thermal expansion coefficient, and ν denotes the kinematic viscosity of the fluid. By examining the velocity and temperature fluctuations, Cheesewright (1968) identified the onset of laminar–turbulent transition at $Gr_x = 2 \times 10^9$, and the beginning of the turbulent regime at $Gr_x = 2 \times 10^{10}$. In the turbulent regime, the Nusselt number, which characterises the wall heat transfer rate of the flow, was found to follow a 0.33 power law with Grashof number as suggested by Bayley (1955). Similar results were also seen in Warner & Arpaci (1968), where the NCBL was considered turbulent for $Gr_x > 8 \times 10^9$ based on their thermocouple measurements up to $Gr_x = 10^{11}$. Siebers, Moffatt & Schwind (1985) studied the heat transfer characteristics of a turbulent NCBL up to $Gr_x = 10^{12}$, with maximum temperature difference 500 °C. Their measurements showed that the laminar–turbulent transition is greatly affected by the variations in fluid properties due to large temperature differences, and the heat transfer in the turbulent regime follows a $1/3$ power law with a reference temperature correction. Tsuji & Nagano (1988*a*) investigated a spatially developing turbulent NCBL with detailed experiment measurements for turbulence statistics up to $Gr_x = 1.8 \times 10^{11}$. Using the experiment data, Tsuji & Nagano (1988*a*) found that their spatially developing NCBL undergoes transition at $Gr_x \approx 8 \times 10^8$, and a turbulent regime was identified for $Gr_x > 7 \times 10^9$ based on the mean velocity and temperature profiles. Their measurements of the Nusselt number in the turbulent regime were found to follow an empirical $1/3$ power law correlation with the Grashof number, which is consistent with studies in the similar Grashof number range ($Gr_x < O(10^{11})$; Saunders 1936, 1939; Bayley 1955; Cheesewright 1968; Siebers *et al.* 1985; Nakao, Hattori & Suto 2017). Their work was extended further by Tsuji & Nagano (1989), who related empirically the boundary layer thickness δ to the downstream distance x. This δ–x correlation enables the comparison between statistically steady NCBL flows and the temporally evolving periodic flows by matching the boundary layer thickness. Abedin, Tsuji & Hattori (2009) compared their direct numerical simulations (DNS) for a temporally developing NCBL with the measurements of Tsuji & Nagano (1988*a*) by matching the boundary layer thickness at $Gr_\delta = 5.94 \times 10^6$. Although initial conditions were shown to

have significant effects on the turbulence statistics in their study, the ensemble average of multiple DNS with different initialisations showed good agreement with the data of Tsuji & Nagano (1988*a*). To date, most existing studies for turbulent vertical NCBLs sit within the range from $Gr_\delta = 2 \times 10^5$ (equivalently, $Gr_x = 10^9$ for spatially developing measurements) to $Gr_\delta = 6.5 \times 10^6$ (equivalently, $Gr_x = 10^{11}$).

More recently, evidence suggests that the turbulent NCBL flow immediately after the laminar–turbulent transition has a laminar near-wall flow with a turbulent outer shear layer (e.g. Wells & Worster 2008; Ng *et al.* 2015, 2017). This is consistent with the idea of an ultimate turbulent regime that has been well developed in Rayleigh–Bénard convection (Grossmann & Lohse 2000, 2011), where the development of turbulence is comprised of two stages: a background-dominated regime where the flow is in fact a laminar boundary layer driven by a turbulent bulk 'wind', and an ultimate regime where both boundary layer and the bulk 'wind' are fully turbulent. In the context of vertical convection flows, the transition towards the ultimate regime for turbulent NCBL flows indeed requires the near-wall laminar-like boundary layer to evolve into a fully turbulent one (Kraichnan 1962; Grossmann & Lohse 2000, 2011). However, while the turbulence statistics of the turbulent NCBL have been well documented for flows at laboratory scale (i.e. $Gr_\delta < O(10^7)$), significantly fewer data extend to sufficiently high Grashof number to see a transition to the ultimate regime. Therefore, the extent and characteristics of the initial laminar-like turbulent regime, as well as the details of this transition towards the ultimate regime, are not well understood. Ng *et al.* (2015) studied numerically the natural convection with Prandtl number $Pr = 0.709$ in a differentially heated channel up to a channel-width-based Grashof number $Gr_H = 1.41 \times 10^9$. In their analysis, they treated the NCBL in two separate parts – an outer bulk flow driven by a turbulent 'wind', and an inner boundary layer. Using DNS data, they showed that although the outer bulk flow is identified as fully developed turbulence, the inner boundary layer could still be laminar-like and follows a Prandtl–Blasius–Pohlhausen scaling. This multi-layer approach for the turbulent NCBL conveniently distinguishes the near-wall characteristics from the bulk flow behaviour where the viscous force and molecular diffusion are negligible, and allows asymptotic matching between the layers to give explicit expressions for the mean temperature and velocity profiles (George & Capp 1979; Hölling & Herwig 2005; Shiri & George 2008). Their work was later extended by Ng *et al.* (2017), where the authors conditionally averaged the turbulence statistics based on high- and low-shear patches in the near-wall region, and recovered a 0.37 power law for the Nusselt number correlation in high-shear events. With increasing Grashof number, Ng *et al.* (2017) showed that the high-shear patches occupy increasingly larger portions of the wall areas, and suggested that the flow would transition to an ultimate shear-dominated regime at higher Grashof number. A similar idea is seen in Wells & Worster (2008), where they conceptually decomposed a spatially developing NCBL into a two-layer structure in their theoretical analysis. Based on empirical correlations for the forced flow, and making use of the measurements of Tsuji & Nagano (1988*a*,*b*), Wells & Worster (2008) suggested that the turbulent NCBL would have two distinct stages as the flow progressively becomes more turbulent: at relatively low Grashof number, the flow is dominated by the near-wall buoyancy as in Tsuji & Nagano (1988*a*), whereas at higher Grashof number, the flow would be dominated by inertia since the near-wall buoyancy grows thin. Using a Reynolds analogy, Wells & Worster (2008) further suggested that the Nusselt number at asymptotically high Grashof number ($Gr_\delta > O(10^{11})$) would follow a $1/2$ power law.

In temporally developing periodic DNS, Ke *et al.* (2020) demonstrated that for $Gr_\delta > 10^7$, the NCBL flow would become fully turbulent such that a universal buoyancy-modified log law is obtained, whereas at relatively low Grashof number $10^6 < Gr_\delta < 10^7$, where the NCBL is generally thought to be turbulent in the literature, the flow is still transitional or weakly turbulent. Ke *et al.* (2021) further explored the flow characteristics and turbulence structures by separating the turbulent flow into a near-wall boundary-layer-like region and an outer plume-like region using the maximum mean streamwise velocity location δ_m. In the fully turbulent regime, there exists a constant heat flux layer (e.g. George & Capp 1979; Hölling & Herwig 2005) and a constant forcing layer in the near-wall region, while the outer plume-like region appears self-similar and can be well modelled by an integral plume model (cf. Morton, Taylor & Turner 1956; Cooper & Hunt 2010). Using DNS data, Ke *et al.* (2021) showed that the local heat transfer in the plume-like region exhibits a $1/2$ power law to the local plume Grashof number, similar to the asymptotic heat transfer in Grossmann & Lohse (2000) and Wells & Worster (2008), while the overall Nusselt number would follow a fully turbulent scaling with logarithmic correction due to the near-wall kinetic boundary layer (resulting in a 0.381 power law for $10^7 < Gr_\delta < 1.2 \times 10^8$), consistent with Grossmann & Lohse (2011) and Ng *et al.* (2017). The authors also noted that the departure from the empirical $1/3$ power law to the slightly higher 0.381 power scaling at $Gr_\delta > 10^7$ is very subtle and gradual. A similar multi-layer approach is also seen in Wei, Wang & Abraham (2021*a*,*b*), where, using the measurements of Tsuji & Nagano (1988*a*,*b*), they showed that the near-wall region of the NCBL is similar to that of a differentially heated channel flow, while the outer part of the NCBL is similar to that of a turbulent planar plume. Howland *et al.* (2022) studied natural convection in differentially heated channels at high Prandtl numbers using DNS. Following Wells & Worster (2008), they used empirical relations for the forced flows to estimate the Prandtl number dependence on the transition to the shear-driven ultimate regime. So far, investigations on the turbulence development in the relatively low Grashof number regime has been limited since the turbulent flow at this stage appears transitional or weakly turbulent, largely dependent on the initial conditions. Early studies did not differentiate between a fully turbulent NCBL and the one that is turbulent in the outer plume-like region but laminar in the near-wall region – hereafter, the 'classical' turbulent regime, since most early studies would seem to be in this regime based on their turbulence statistics (see § 3.1), given their subtle difference in the Nusselt number scaling and lack of direct measurements of high Grashof number flows with which to compare. Now that fully turbulent results have been obtained, it is possible to re-examine the near-wall mechanics on the 'classical' weakly turbulent regime and clarify how and when near-wall transition takes place.

The present study investigates a turbulent NCBL flow with Prandtl number 0.71 using periodic temporally developing DNS, focusing on the development of turbulence in such a 'classical' turbulent regime. By comparing the turbulence statistics in § 3.1 and the premultiplied power spectra in § 3.2, we will show that the near-wall region is initially laminar-like, and the turbulent NCBL is indeed driven by the bulk plume-like structures. Using a dimensionless length scale, the extent of the 'classical' turbulent regime can be identified in § 3.3. In this regime, the skin friction coefficient follows a laminar-like scaling as in Blasius boundary layers, whereas at higher Grashof number, the flow appears initial-condition-invariant, and the skin friction converges to a more complicated log-law-type behaviour. In § 3.4, we explore the development of the near-wall turbulence by examining the turbulence kinetic energy budget in both the 'classical' and fully turbulent ultimate regimes. Section 4 briefly concludes the findings in this paper.

2. Mathematical description

The evolution of the incompressible natural convection flow is comprised of the conservation equations of mass, momentum and thermal energy. With the Boussinesq approximation, the governing equations read

$$\frac{\partial u_i}{\partial x_i} = 0, \tag{2.1a}$$

$$\frac{\partial u_i}{\partial t} + \frac{\partial u_i u_j}{\partial x_j} = -\frac{1}{\rho}\frac{\partial p}{\partial x_i} + \nu \frac{\partial^2 u_i}{\partial {x_j}^2} + g\beta\theta\delta_{i1}, \tag{2.1b}$$

$$\frac{\partial \theta}{\partial t} + \frac{\partial u_j \theta}{\partial x_j} = \kappa \frac{\partial^2 \theta}{\partial {x_j}^2}, \tag{2.1c}$$

where the subscripts $i, j = 1, 2, 3$ denote the velocity field u in the x (streamwise), y (wall-normal) and z (spanwise) directions. In (2.1), ρ is the density of the fluid, g represents the projection of the gravitational vector pointing in the negative x direction, $\theta = T - T_\infty$ is the temperature difference between the local temperature T and the far-field temperature T_∞, and δ_{i1} is the Kronecker delta. Also, β, κ and ν are the fluid properties: the thermal expansion coefficient, the thermal diffusivity and the kinematic viscosity, respectively. For the problem under consideration, the working fluid is considered as air with Prandtl number $Pr \equiv \nu/\kappa = 0.71$.

To allow a spatially invariant, temporal flow to develop, periodic boundary conditions are applied in the streamwise and spanwise directions. For the wall-normal direction, no-slip and no-permeability conditions are imposed on the isothermal wall ($\theta = \theta_w$ at $y = 0$) and a slip wall boundary is applied in the quiescent far field ($\theta = 0$ at $y = \infty$).

With these boundary conditions, the flow system (2.1) has a laminar analytical solution (Illingworth 1950; Schetz & Eichhorn 1962) that reads

$$u(\eta) = \frac{4g\beta\theta_w t}{1 - Pr}\left[\mathrm{i}^2\mathrm{erfc}(\eta) - \mathrm{i}^2\mathrm{erfc}\left(\frac{\eta}{\sqrt{Pr}}\right)\right], \tag{2.2a}$$

$$\theta(\eta) = \theta_w\,\mathrm{erfc}(\eta), \tag{2.2b}$$

where u is the streamwise velocity (note that the parallel flow is streamwise- and spanwise-invariant), $\mathrm{erfc}(\eta)$ is the complementary error function of the similarity coordinate $\eta = y/\sqrt{4\kappa t}$, and $\mathrm{i}^n\mathrm{erfc}(\eta)$ represents the nth integral of the complementary error function: $\mathrm{ierfc}(\eta) = \int_\eta^\infty \mathrm{erfc}(\eta)\,\mathrm{d}\eta = \exp(-\eta^2)/\sqrt{\pi} - \eta\,\mathrm{erfc}(\eta)$ and $\mathrm{i}^2\mathrm{erfc}(\eta) = (\mathrm{erfc}(\eta) - 2\eta\,\mathrm{ierfc}(\eta))/4$.

To encourage a three-dimensional transition to turbulence, the laminar temperature field (2.2*b*) is also augmented with a perturbation, such that the initial temperature field θ_0 is given by

$$\theta_0(x, y, z) = \theta(y) + \tilde{\theta}(x, y, z), \tag{2.3}$$

where $\theta(y)$ is the laminar analytical solution obtained from (2.2*b*), the perturbation $\tilde{\theta}(x, y, z)$ is defined by

$$\tilde{\theta}(x, y, z) = A_0[\mathrm{RAND}(0, 1) - 0.5], \tag{2.4}$$

$A_0 = 1$ denotes the magnitude of the background white noise, and RAND(0, 1) is a statistically uniform random number generator between 0 and 1. The flow is initialised

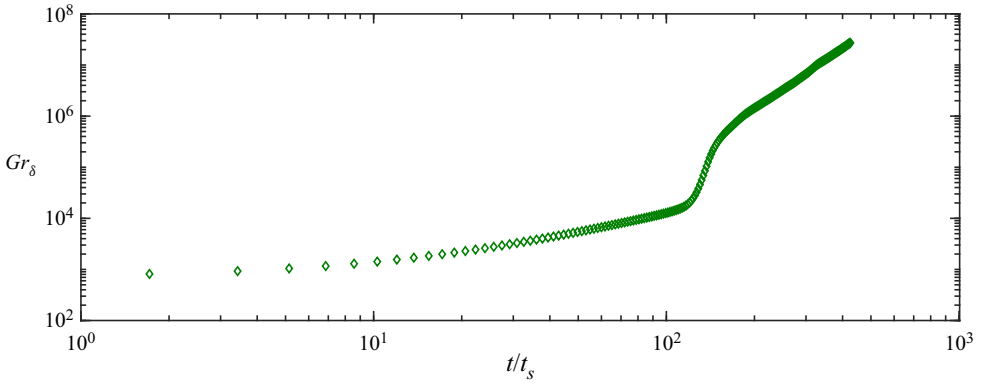

Figure 1. The Grashof number Gr_δ evolution of the NCBL (for DNS-D) with the flow development time t/t_s, where $t_s = \kappa^{1/3}/(g\beta\theta_w)^{2/3}$ is the intrinsic time scale.

using the velocity analytical solution (2.2*a*) and the perturbed temperature field (2.3) at $Gr_{\delta_0} = 705$. Here, the Grashof number Gr_δ and the integral velocity boundary layer thickness δ are given as

$$Gr_\delta \equiv \frac{g\beta\theta_w\delta^3}{\nu^2}, \quad \delta \equiv \int_0^\infty \frac{\bar{u}}{\bar{u}_m}\,\mathrm{d}y, \tag{2.5a,b}$$

where $\bar{u}$ represents the mean (spatial average) quantity of the streamwise velocity u in the homogeneous x–z plane, and $\bar{u}_m$ denotes the maximum mean streamwise velocity. Note that our temporally developing NCBL is streamwise- and spanwise-invariant such that the boundary layer thickness δ and Grashof number Gr_δ are proxies for the flow development time t, as shown in figure 1. Although the magnitude of initial noise $A_0 = 1$ is relatively large, the artificial temperature perturbation decays rapidly via the receptivity process after a few iterations, and the noise modes in the laminar regime grow linearly in accordance with linear stability results before they undergo nonlinear amplification (Ke *et al.* 2019).

The DNS are carried out on a Cartesian finite volume grid, with a uniform mesh in the homogeneous directions (streamwise and spanwise), while the wall-normal direction employs a logarithmically stretched mesh using a gamma function (table 1). The grid sizes are determined so that they are able to resolve the Kolmogorov scales by the end of the simulation (cf. Ng *et al.* 2015; Williamson *et al.* 2015), with $\Delta x \approx \Delta z \approx 2.5\eta_k$ in the homogeneous directions, and $\Delta y_{min} \approx 0.3\eta_k$ and $\Delta y_{max} \approx 6.4\eta_k$ in the wall-normal direction. Here, $\eta_k = (-\nu^3/\varepsilon)^{1/4}$ is the Kolmogorov length scale, and $\varepsilon = -\nu\,\overline{(\partial u_i'/\partial x_j)}$ is the turbulent dissipation. In the following analysis, we also include the DNS data that have been reported previously in Ke *et al.* (2020, 2021) for comparison; the detailed initial conditions for these simulations are listed in table 2. We will show in § 3 that these initial conditions are responsible for different transition pathways that the NCBLs undergo, but have minimal effect on the flow statistics once the flow becomes fully turbulent in the ultimate regime.

In the present study, the turbulence statistics of our temporally developing NCBL are compared with the spatially developing NCBL flows (Tsuji & Nagano 1988*a*; Nakao *et al.* 2017) by matching the boundary layer thickness δ. This method has also been adopted by a number of studies for the temporally developing NCBL (Abedin *et al.* 2009; Ke *et al.* 2020, 2021). It is noted that for spatially developing NCBL flows, statistics are normally obtained by taking the temporal average since the flow is steady in the mean, whereas

Direction	Domain size L	Grids N	L/δ_f	$\Delta^{\eta_k}_{min}$	$\Delta^{\eta_k}_{max}$	Δ^{+}_{min}	Δ^{+}_{max}
x	$3520L_s$	2750	14.74	2.52	2.52	4.71	4.71
y	$828L_s$	800	3.47	0.326	6.41	0.61	11.98
z	$828L_s$	650	3.47	2.51	2.51	4.69	4.69

Table 1. Simulation parameters for the present study (DNS-D). Here, $L_s = \kappa^{2/3}/(g\beta\theta_w)^{1/3}$ is the intrinsic length scale, δ_f represents the velocity integral thickness by the end of the simulation, Δ^{η_k} and Δ^{+} denote the grid size in Kolmogorov scale and wall units by the end of the simulation, with the subscripts *min* and *max* indicating the smallest grid (first grid on the wall) and the largest grid (far field).

Case	Source	Initial Gr_{δ_0}	Initial temperature field θ_0
DNS-A	Ke *et al.* (2020)	3000	$\theta_0 = \bar{\theta}(y) + \tilde{\theta}_{xz}$
DNS-C	Ke *et al.* (2021)	5×10^7	DNS-A
DNS-D	Present study	705	(2.3)

Table 2. Initial conditions for the DNS dataset. Here, $\tilde{\theta}_{xz}$ is a discrete sinusoidal perturbation in both the streamwise and spanwise directions (cf. Ke *et al.* 2020).

for our temporally developing NCBL, the parallel flow is unsteady in the mean and the statistics are obtained by averaging over the homogeneous x–z plane.

3. Results and discussion

The characteristics of high Grashof number flows that transition to the ultimate regime have been investigated extensively in our earlier analyses (Ke *et al.* 2020, 2021), and we will focus primarily on the 'classical' (weakly turbulent) regime in the following analysis.

Before proceeding to the detailed analysis, a rigorous identification of the near-wall region is needed. Following our earlier analysis (Ke *et al.* 2021), we identify the near-wall and outer bulk region of the NCBL flow by the maximum mean streamwise velocity location δ_m. This wall-normal location distinguishes turbulence behaviours in the two shear layers of the NCBL: figure 2 shows the ratio of the streamwise (λ_f) to the spanwise (λ_g) Taylor microscale, which are obtained by using the mean autocorrelation in the respective directions, at three Grashof numbers in the turbulent regime ($Gr_\delta > 10^6$ for DNS-D; see § 3.1). Beyond the maximum mean streamwise velocity location ($y > \delta_m$), $\lambda_f/\lambda_g \approx \sqrt{2}$ is approximately constant for all data shown in figure 2, indicating that the flow in this region is isotropic due to strong turbulent mixing (Pope 2001), whereas in the near-wall region ($y < \delta_m$), λ_f/λ_g grows with Gr_δ and shows a strongly anisotropic behaviour as would have been seen in turbulent boundary layer flows.

3.1. *Mean statistics*

The dimensionless wall heat flux of the flow is expressed by the Nusselt number, given by

$$Nu_\delta = \frac{q_w \delta}{\rho C_p \kappa \theta_w}, \tag{3.1}$$

where C_p denotes the specific heat capacity of the fluid, and $q_w = -\rho C_p \kappa\, (\partial\bar{\theta}/\partial y)_{y=0}$ is the wall heat flux. Figure 3 compares the Nusselt number development of our temporally

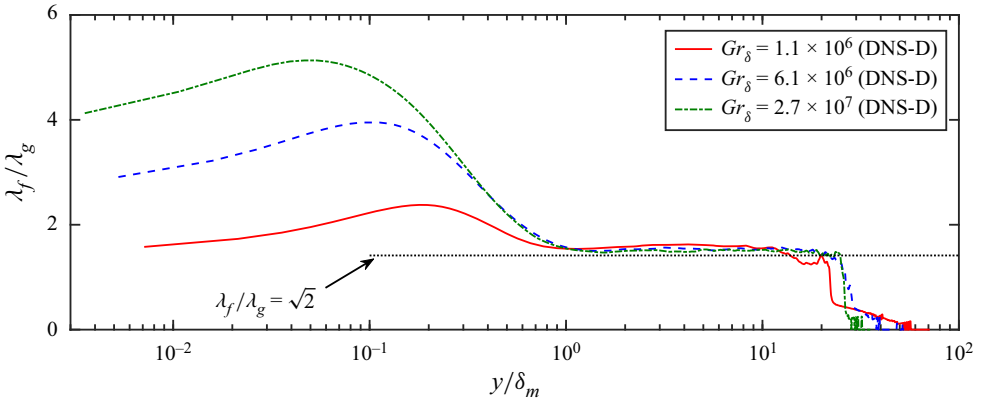

Figure 2. Ratio of the streamwise Taylor microscale λ_f to its spanwise counterpart λ_g for DNS-D.

developing DNS with existing measurements for spatially developing flows (Tsuji & Nagano 1988*a*; Nakao *et al.* 2017) and the ensemble average of multiple temporal flows with different initialisations (Abedin *et al.* 2009). From figure 3, DNS-D demonstrates good agreement with the statistically steady measurements of Abedin *et al.* (2009) and undergoes turbulent transition at $Gr_\delta \approx 10^6$. We stress that it is difficult to determine an accurate starting point of a 'turbulent' regime in the classical sense as the transition process towards turbulence is gradual and the oscillations in flow statistics also exacerbate the difficulty in detecting this starting point accurately. Here, we have adopted $Gr_\delta \approx 10^6$ to be the starting point of turbulence for DNS-D, so it is consistent with previous studies (e.g. Tsuji & Nagano 1988*a*; Abedin *et al.* 2009) due to the similar trend seen in the Nusselt number. Immediately after the transition, DNS-D also shows a Nu_δ–Gr_δ trend similar to the spatially developing measurements, which closely follows the 'classical' empirical correlation suggested by Tsuji & Nagano (1988*a*):

$$Nu_\delta = 0.107\, Gr_\delta^{1/3}, \tag{3.2}$$

for $10^6 < Gr_\delta < 10^7$. However, such a 'classical' 1/3 power law is not observable for DNS-A in this Grashof number range due to a different initialisation: in DNS-A, we have employed a discrete sinusoidal perturbation that includes the most amplified streamwise and spanwise modes as described by Ke *et al.* (2019, 2020). Such a discrete perturbation leads to a laminar–turbulent transition pathway different from DNS-D: DNS-A has an extended transition region, with more energetic three-dimensional structures in the outer bulk flow, which leads to larger oscillations apparent in Nu_δ shown in figure 3. Similar observation of the initial condition effect on flow transition and statistics has also been reported and discussed in our previous investigation (cf. figure 2 in Ke *et al.* 2020). As a result, DNS-A bypasses the 'classical' turbulent regime and remains strongly transitional (such that the flow statistics depend heavily on the initial condition) until a higher Grashof number ($Gr_\delta = 10^7$) is reached. On the other hand, in DNS-D, the flow is perturbed with a broadband random white noise that appears more comparable with the laboratory conditions (Tsuji & Nagano 1988*a*) and the ensemble average of multiple initialisations (Abedin *et al.* 2009). Nevertheless, at higher Grashof number in the turbulent regime ($Gr_\delta > 10^7$) DNS-D collapses on DNS-A, suggesting that both flows become fully turbulent and initial-condition-invariant, and follow a 0.381 power law as suggested by Ke *et al.* (2021). This 0.381 power law is slightly higher than the empirical

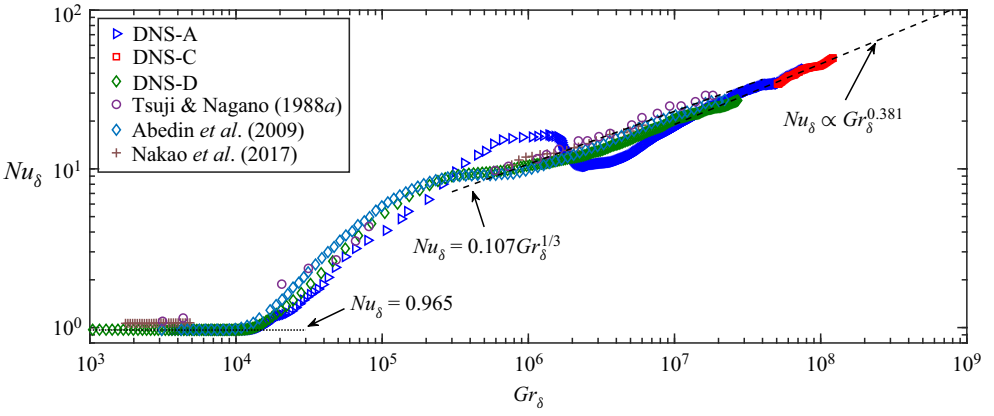

Figure 3. Nusselt number development of the NCBL. The black dotted line represents the laminar analytical value $Nu_\delta = 0.965$ (Ke *et al.* 2019), and the black dashed lines indicate the empirical $1/3$ power law correlation for the 'classical' regime, and the 0.381 power law for the fully turbulent regime (Ke *et al.* 2021).

correlation (3.2) in the 'classical' turbulent regime, but is consistent with the ultimate heat transfer (Grossmann & Lohse 2000; Ng *et al.* 2017) with a logarithmic correction due to the turbulent kinetic boundary layer (Grossmann & Lohse 2011; Ke *et al.* 2021).

The mean streamwise velocity u^+ and temperature θ^+ profiles for the NCBL are shown in figure 4 in wall units. Here, the mean profiles u^+ and θ^+ are given by

$$u^+ = \frac{\bar{u}}{u_\tau}, \quad \theta^+ = \frac{\theta_w - \bar{\theta}}{\theta_\tau}, \tag{3.3a,b}$$

and the friction quantities are given by the wall shear stress $\tau_w = \rho\nu\,(\partial\bar{u}/\partial y)_{y=0}$ and wall heat flux q_w:

$$u_\tau = \sqrt{\tau_w/\rho}, \quad \theta_\tau = \frac{q_w}{\rho C_p u_\tau}. \tag{3.4a,b}$$

Evidently, both profiles demonstrate a strong dependence on the flow development at relatively low Grashof number ($Gr_\delta < O(10^7)$ for our DNS data): as the flow progressively achieves higher Gr_δ in this 'classical' regime, both mean statistics shift upwards with increasing magnitude, which highlights the absence of a universal logarithmic behaviour that is commonly found in the canonical forced flows. A similar observation is also seen in previous NCBL studies (e.g. Tsuji & Nagano 1988*a*; Ng *et al.* 2017). As shown in figure 4(*a*), the velocity profiles of DNS-D at $Gr_\delta = 1.1 \times 10^6$ and 6.1×10^6 demonstrate reasonably good agreement with the published measurements (Tsuji & Nagano 1988*a*; Abedin *et al.* 2009; Nakao *et al.* 2017), whilst the temperature profiles in figure 4(*b*) shows good qualitative agreement with the existing data. Note that here we do not expect our data to collapse with the existing data precisely as we are comparing the temporally developing NCBL with the spatially developing flows at different Gr_δ. It is also noted that the mean statistics at this stage, being weakly turbulent, still depend largely on how the flow undergoes laminar–turbulent transition and therefore the initial conditions (see e.g. Ke *et al.* (2020) for the statistics of DNS-B). Such an initial condition dependence has been minimised in Abedin *et al.* (2009) – since they have used an ensemble average of DNS data with a number of different initialisations to obtain statistics – and also in the steady-state spatial measurements of Tsuji & Nagano (1988*a*) and Nakao *et al.* (2017).

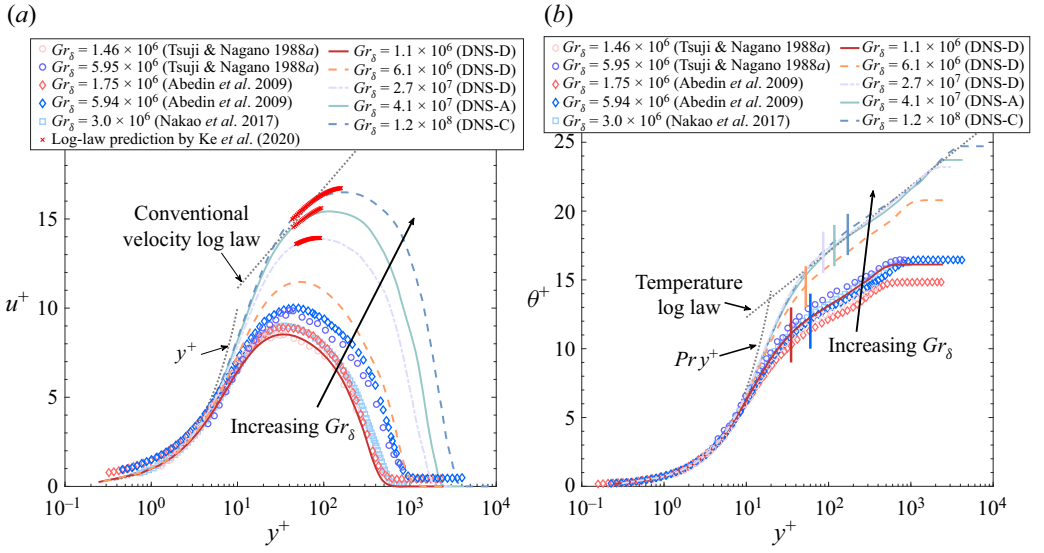

Figure 4. The mean profiles of (*a*) streamwise velocity and (*b*) temperature, for the NCBL at different Gr_δ. Symbols indicate the mean profiles obtained from other sources: circles are experiment measurements of Tsuji & Nagano (1988*a*) for a spatially developing NCBL; diamonds are ensemble averages of DNS data by Abedin *et al.* (2009) for temporally developing NCBLs; squares are large-eddy simulation data of Nakao *et al.* (2017) for a spatially developing NCBL. Red crosses in (*a*) represent the buoyancy-modified velocity log law proposed by Ke *et al.* (2020) in the range $50 < y^+ < \delta_m^+$. Coloured vertical lines in (*b*) indicate the δ_m locations for the corresponding DNS data, with blue representing the largest δ_m location for the published data, i.e. $Gr_\delta \approx 6 \times 10^6$ ($\delta_m^+ \approx 60$) for Abedin *et al.* (2009) and Tsuji & Nagano (1988*a*).

At sufficiently high Grashof number ($Gr_\delta > O(10^7)$ for our DNS data), the NCBL flow gradually transitions to the so-called ultimate regime. With reference to figure 4, during this process the temperature profiles become initial-condition-invariant and collapse onto a universal temperature log law (cf. Ke *et al.* 2020), whereas the mean streamwise velocity profiles also start to follow a buoyancy-modified log law (cf. Ke *et al.* 2020). We also note that this temperature log law sits primarily in the outer bulk plume-like region beyond the velocity maximum location (i.e. outside the boundary layer; see coloured vertical lines in figure 4*b*), which is distinct from the velocity log law that sits within the boundary layer for forced flows. The detailed insight of the flow statistics in the ultimate regime have been discussed in our previous investigations (Ke *et al.* 2020, 2021); here, we focus on the regime spanning the transition of the near-wall region to turbulence.

To further investigate the near-wall turbulence mechanism of the NCBL flow, the Reynolds stresses normalised by the friction velocity u_τ are also assessed in figure 5. As shown in figure 5(*a*), the normalised Reynolds shear stress $\overline{u'v'}/u_\tau^2$ for our DNS data in the 'classical' regime (DNS-D at $Gr_\delta = 1.1 \times 10^6$ and 6.1×10^6) shows relatively good agreement with the existing measurements in the similar Gr_δ range. Our conception is that at relatively low Gr_δ, the NCBL flow is in a state where the outer bulk flow is turbulent, while the near-wall region is only weakly turbulent or laminar as reported for channel flows (Ng *et al.* 2015, 2017). In this regime, the momentum transport through turbulent mixing is negligible, and the Reynolds shear $\overline{u'v'}$ may be small or zero in magnitude

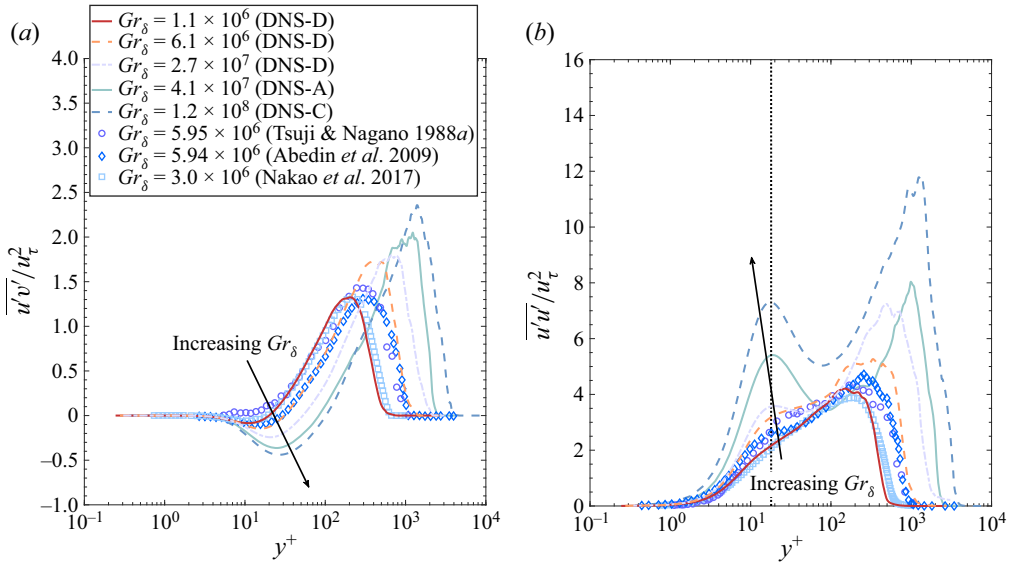

Figure 5. Normalised profiles of (*a*) Reynolds shear stress $\overline{u'v'}$ and (*b*) streamwise normal stress $\overline{u'u'}$, in wall units.

near the wall, as seen in figure 5(*a*): our DNS data show a negative trough for $y^+ \approx 12$ ($Gr_\delta = 1.1 \times 10^6$) and $y^+ \approx 17$ ($Gr_\delta = 6.1 \times 10^6$), and a similar slightly negative site in the near-wall region is also captured in the temporal DNS by Abedin *et al.* (2009). Such a negative near-wall $\overline{u'v'}$ region has also been observed in Ortiz, Koloszar & Planquart (2019) for a small Prandtl number turbulent NCBL flow. However, the measurements for the spatially developing NCBL flows (Tsuji & Nagano 1988*a*; Nakao *et al.* 2017) are nearly zero in the near-wall region. With increasing Gr_δ, the near-wall negative trough of the Reynolds shear stress grows in magnitude since the momentum transport through turbulent mixing becomes stronger. A similar trend is also seen in a more recent DNS study for a NCBL in a differentially heated vertical channel by Kim, Ahn & Choi (2021), where they illustrated that the near-wall negative site of the Reynolds shear stress becomes evident only at sufficiently high Grashof number flow, and the magnitude of the negative trough progressively becomes larger with increased Grashof number.

This idea is further supported by the normalised streamwise normal stress $\overline{u'u'}$ profile in figure 5(*b*). At relatively low Gr_δ, our DNS data collapse reasonably well with the existing measurements. As the flow progressively achieves higher Gr_δ, the $\overline{u'u'}$ profile gradually develops from a mono-peak profile into a dual-peak structure. The two local peaks essentially represent the two shear layers in the near-wall boundary-layer-like region and the outer bulk (i.e. plume-like) region, similar to that of the planar jet flows (e.g. Naqavi, Tyacke & Tucker 2018). The inner peak location for $\overline{u'u'}$ occurs at $y^+ \approx 18$ (represented by the black dotted line in figure 5*b*), and shows minimal Gr_δ dependence for the data presented, whereas its magnitude grows with increasing Gr_δ. Similar peak magnitude dependence on the flow development for turbulence intensities is also seen in momentum-driven wall-bounded flows (Wei & Willmarth 1989; Antonia *et al.* 1992; Marusic, Uddin & Perry 1997; Moser, Kim & Mansour 1999). As shown in figure 5(*b*), this inner peak is not as evident for the literature measurements and our DNS data up to

$Gr_\delta \approx 6 \times 10^6$ since at this stage the near-wall region is not yet turbulent in the sense of von Kármán.

3.2. *Turbulence structure*

The development of such an energetic signature of the near-wall turbulence structure can be seen more clearly in the premultiplied spectra of the streamwise velocity fluctuation ($k_x E_{uu}$) across the wall-normal direction in figure 6. The premultiplied form of the power spectra conveniently visualises the energy contribution from various length scales. In figure 6, E_{uu} is the one-dimensional power spectra of the streamwise velocity fluctuation u', $k_x = 2\pi/\lambda_x$ is the streamwise wavenumber, $\lambda_x^+ = \lambda_x u_\tau/\nu$ is the streamwise wavelength in wall units, and δ_m denotes the maximum mean streamwise velocity location. We note that although the contour of the premultiplied spectra at higher Grashof number in figure 6(*b*) is not fully enclosed and therefore has missed the energy contributions from wavelengths greater than the domain size, the use of a truncated domain has been used in canonical wall-bounded turbulent flows and was shown to be efficient to capture the near-wall statistics (e.g. Del Alamo *et al.* 2004; MacDonald *et al.* 2017). The key feature that we wish to highlight here is the spectral difference between the flows in the two regimes, especially in the near-wall region.

For the weakly turbulent flow shown in figure 6(*a*), a clear peak in the premultiplied spectra contour emerges at $y/\delta_m \approx 7$ (shown in the red dash-dotted lines) and $\lambda_x/\delta_m \approx 45$, while the premultiplied spectra quickly decays to zero in the near-wall region. For canonical wall-bounded turbulence, such an 'outer' site of the energy usually occurs in the logarithmic region within the boundary layer at sufficiently high Reynolds number (cf. Hutchins & Marusic (2007*b*); Mathis, Hutchins & Marusic (2009) for the superstructure of the very-large-scale motions), whereas in our NCBL flow, this energy site is associated with the shear layer in the plume-like outer bulk (outside the near-wall boundary layer) and appears prominent at relatively low Gr_δ. This result suggests that although the flow is turbulent in the outer plume-like region ($y > \delta_m$), it is not turbulent enough to generate an energetic peak in the near-wall region ($y < \delta_m$), which is linked directly to the wall turbulence kinetic energy production. At higher Gr_δ, the near-wall peak site starts to emerge, as shown in figure 6(*b*), and the premultiplied spectra contour demonstrates a bimodal composition as seen in turbulent boundary layers (Hutchins & Marusic 2007*b*) and wall jet flows (Gnanamanickam *et al.* 2019). Both inner and outer sites (normalised with u_τ) were observed to grow in magnitude with increasing Gr_δ for our temporally developing NCBL, similar to the observations seen in the forced flows (Hutchins & Marusic 2007*a*; Mathis *et al.* 2009; Gnanamanickam *et al.* 2019; although the outer sites for the forced flows are due to superstructures of very-large-scale motions rather than the additional shear layer). As shown in figure 6(*b*), the near-wall site at $Gr_\delta = 2.7 \times 10^7$ has peak magnitude $k_x E_{uu}/u_\tau^2 \approx 0.8$ for DNS-D, and for DNS-A it is $k_x E_{uu}/u_\tau^2 \approx 4.2$ at $Gr_\delta = 7.7 \times 10^7$. To compare the spectra distribution with canonical wall-bounded turbulent flows, in figure 6(*b*) we also include the near-wall contours at $k_x E_{uu}/u_\tau^2 = 1.2$ for the DNS data of a channel flow (cf. Del Alamo *et al.* 2004) at $Re_\tau = 934$ (based on the channel half-width) and the measurements of a turbulent boundary layer (cf. Hutchins & Marusic 2007*b*, figure 3) at $Re_\tau = 7300$ (based on the boundary layer thickness). Notably, although for DNS-D the near-wall energy site at $Gr_\delta = 2.7 \times 10^7$ has a lower peak magnitude ($k_x E_{uu}/u_\tau^2 = 0.8$) than those of the reported forced flow data due to a much lower Reynolds number ($Re_\tau \approx 85$ based on the maximum mean streamwise velocity location δ_m; also note that the normalisation with u_τ does not take

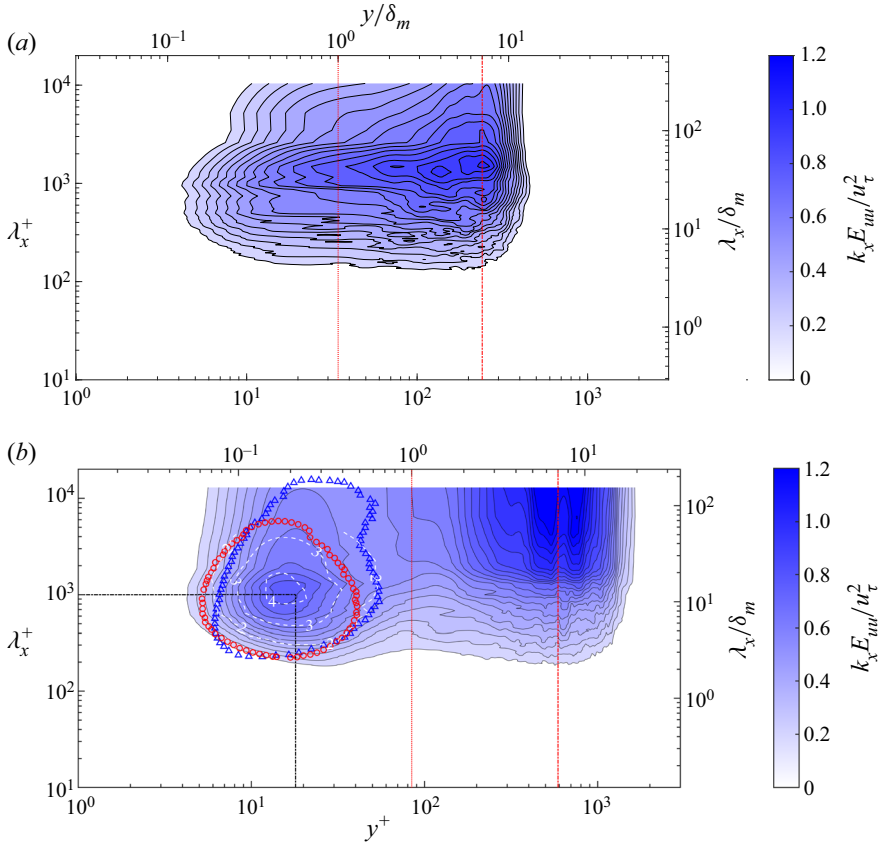

Figure 6. Normalised premultiplied spectra contours of streamwise fluctuation k_xE_{uu}/u_τ^2 for the turbulent NCBL (DNS-D) in (*a*) the 'classical' regime, $Gr_\delta = 1.1 \times 10^6$ ($Re_\tau \approx 34$), and (*b*) the fully turbulent ultimate regime, $Gr_\delta = 2.7 \times 10^7$ ($Re_\tau \approx 85$). Black dash-dotted lines indicate the inner energy peak site at $\lambda_x^+ \approx 1000$ and $y^+ = 18$; the red dotted line is at the velocity maximum location $y/\delta_m = 1$, which differentiates the near-wall region and the outer bulk flow; the red dash-dotted line indicates the outer energy peak site at $y/\delta_m \approx 7$. White dashed lines indicate contour levels $k_xE_{uu}/u_\tau^2 = 2, 3, 4$ in the near-wall region for DNS-A (Ke *et al.* 2020) at $Gr_\delta = 7.7 \times 10^7$. Red circles indicate the near-wall site contour level $k_xE_{uu}/u_\tau^2 = 1.2$ for a turbulent channel flow at $Re_\tau = 935$ (Del Alamo *et al.* 2004); blue triangles indicate the near-wall site contour level $k_xE_{uu}/u_\tau^2 = 1.2$ for a turbulent boundary layer at $Re_\tau = 7300$ (Hutchins & Marusic 2007*b*).

the near-wall buoyancy into account), it shows a similar distribution to the canonical wall-bounded turbulent flows with a peak centred at $y^+ \approx 18$ and length scale $\lambda_x^+ \approx 1000$ (indicated by black dash-dotted lines in figure 6*b*). This near-wall energetic site is close to the 'inner' energy peak for the turbulence in momentum-driven wall-bounded flows ($y^+ = 15$ and $\lambda_x = 1000$), which corresponds to the near-wall streaks (Kline *et al.* 1967; Hutchins & Marusic 2007*a*,*b*; Ng *et al.* 2017). In contrast to the canonical wall-bounded turbulent flows, where they develop the 'inner' energetic site first and the 'outer' site becomes visible only at sufficiently high Reynolds number (Hutchins & Marusic 2007*b*; Mathis *et al.* 2009), the emerging near-wall energetic site with increasing Gr_δ suggests a different energy development for the NCBL flows: the outer plume-like region becomes turbulent prior to the near-wall boundary-layer-like structures. This observation is consistent with the idea that turbulence development in the NCBL is driven by the

bulk thermal convection in the plume-like structures and limited by the near-wall region (Grossmann & Lohse 2000, 2011; Ke *et al.* 2021).

Similar turbulence development is also seen in the near-wall streak evolution. It is widely acknowledged that for fully developed turbulent wall-bounded flows, the near-wall streaks have constant spacing $\lambda_z^+ \approx 100$–120, which appears largely independent of Reynolds number (Kline *et al.* 1967; Smith & Metzler 1983; Klewicki *et al.* 1995; Tomkins & Adrian 2003; Patel, Boersma & Pecnik 2016), and the mean spacing of the streaks is well represented by the local peak location of the premultiplied spanwise spectra of the streamwise velocity fluctuations. In figure 7(*a*), we present the normalised premultiplied spectra $k_z E_{uu}/u_\tau^2$ at different Grashof numbers at $y^+ \approx 15$ since the merging of streaks are prominent in the region $10 < y^+ < 30$ (Tomkins & Adrian 2003). It can be seen that at relatively low Grashof number ($Gr_\delta = 1.1 \times 10^6$), the normalised premultiplied spectra peaks at $\lambda_z^+ \approx 600$, whereas at higher Grashof number, the peak shifts inwards to $\lambda_z^+ \approx 130$ for both $Gr_\delta = 6.1 \times 10^6$ and $Gr_\delta = 2.7 \times 10^7$. This near-wall energetic signature also occurs at fixed wall coordinates ($\lambda_z^+ \approx 130$ and $y^+ \approx 15$) for our DNS at high Grashof number, which is seen in figure 7(*b*) in the temporal development of the spanwise premultiplied spectra at $y^+ \approx 15$ – as the flow progressively becomes more turbulent, the normalised spanwise spectrum grows in magnitude in this near-wall region, and its peak location agrees with the $\lambda_z^+ = 130$ line (grey dashed). A more quantitative representation of the results presented in figure 7(*b*) can be seen in figure 7(*c*), where the peak location of the spanwise spectra is plotted against Grashof number. In the present study, the peak location is determined by a wavelength band bounded by 90 % of the instantaneous premultiplied spectra maximum at $y^+ \approx 15$ (the 90 % boundaries are indicated by the solid lines in figure 7*c*). As shown in figure 7(*c*), while the peak wavelength band (i.e. the mean streak spacing) is changing appreciably since the flow becomes turbulent at $Gr_\delta = 10^6$; it attains a constant value at $\lambda_z^+ \approx 130$, as would have been seen in the fully turbulent flows (Kline *et al.* 1967; Patel *et al.* 2016) for $Gr_\delta > 6.5 \times 10^6$ (see shaded area in figure 7*c*). Both figures 6 and 7 indicate that the near-wall region is not sufficiently turbulent in the sense of von Kármán at relatively low Grashof number, in which range the NCBL is generally thought turbulent. This constant spacing regime marks the formation of near-wall streaks for the NCBL, and suggests a second stage of the NCBL turbulence development.

This near-wall streak evolution is also clearly seen in the wall-parallel planes of the instantaneous velocity contours in the near-wall region. As shown in figures 8(*a*,*b*), the instantaneous velocity field at $y^+ \approx 15$ develops increasingly finer structures with increasing Gr_δ. While the low-speed packets (coloured blue–white in figure 8) occupy a large wall-parallel area for relatively low Grashof number at $Gr_\delta = 1.1 \times 10^6$ (cf. Ng *et al.* 2017, for non-streaky lower-shear regions), the instantaneous velocity field at $Gr_\delta = 2.7 \times 10^7$ appears much more streaky, with streamwise elongated streaks that are commonly seen in the momentum-driven turbulent boundary layers (e.g. Hutchins & Marusic 2007*a*). Similar observation has been reported by Ng *et al.* (2017) for vertical natural convection in a differentially heated channel. In their analysis, they found that the non-streaky low-speed patches that associate with the low-speed regions decline in size with increasing Grashof number, while the streaky higher-shear regions occupy increasingly larger fractions on the wall areas at higher Grashof number for their steady flows (cf. figures 2 and 3 in Ng *et al.* 2017). Figures 8(*c*,*d*) show magnified views of the blue boxes in figures 8(*a*,*b*), with the horizontal red lines representing the most energetic spanwise wavelengths (λ_z^+ that have the maximum $k_z E_{uu}/u_\tau^2$) indicated by figure 7(*a*).

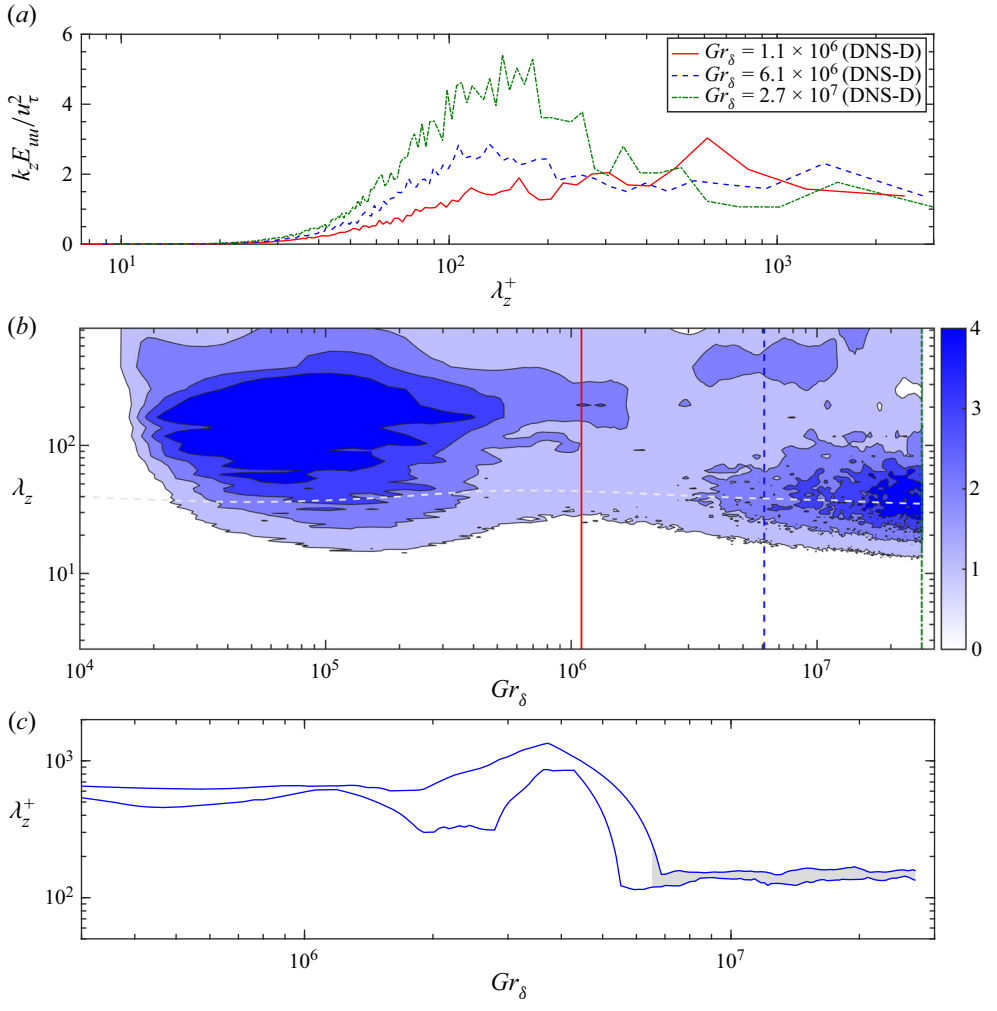

Figure 7. Normalised premultiplied spanwise spectra $k_z E_{uu}/u_\tau^2$ for the turbulent NCBL at $y^+ \approx 15$. (*a*) For different Grashof numbers. (*b*) Contours of the spanwise spectra $k_z E_{uu}/u_\tau^2$ at $y^+ \approx 15$ at various Gr_δ, with coloured vertical lines representing the same information as given in (*a*). (*c*) The temporal development of the instantaneous maximum wavelength band, where the upper and lower lines are the boundaries of the region where $k_z E_{uu}/u_\tau^2$ is greater than 90 % of its instantaneous maximum at $y^+ \approx 15$. The grey dashed line in (*b*) indicates $\lambda_z^+ = 130$, and the shaded area in (*c*) indicates the region $Gr_\delta > 6.5 \times 10^6$ and $k_z E_{uu}/\max(k_z E_{uu}) > 90\,\%$.

It is clear that for $Gr_\delta = 1.1 \times 10^6$, the most energetic spanwise wavelength $\lambda_z^+ \approx 600$ agrees well with the spanwise spacing of the low-speed packets (shown in figure 8*c*), whilst for $Gr_\delta = 2.7 \times 10^7$, the most energetic spanwise wavelength $\lambda_z^+ = 130$ in figure 8(*d*) is representative of the streak spacing (Kline *et al.* 1967; Hutchins & Marusic 2007*a*).

3.3. *Identifying the weakly turbulent regime*

Although figure 7(*c*) provides a convenient way to identify the transition from the 'classical' turbulent to the fully turbulent regime, in this subsection we present an alternative method to distinguish the 'classical' weakly turbulent regime – to show that the

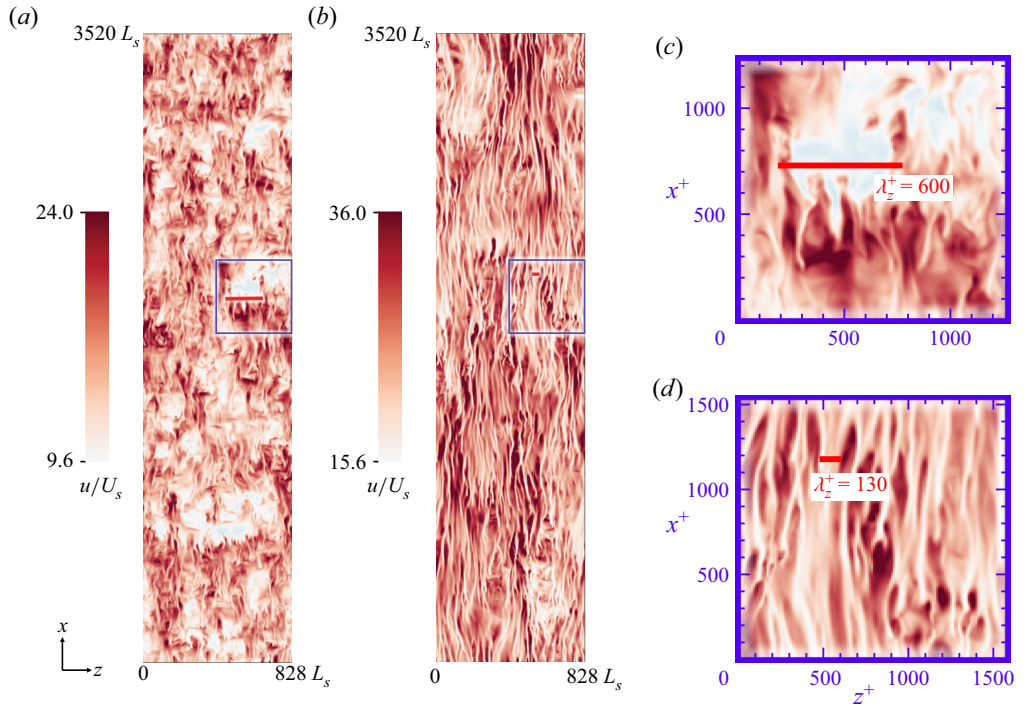

Figure 8. Wall-parallel planes of the normalised instantaneous streamwise velocity u/U_s in the near-wall region at $y^+ \approx 15$ for (*a*) $Gr_\delta = 1.1 \times 10^6$, and (*b*) $Gr_\delta = 2.7 \times 10^7$. Here, $U_s = (\kappa g \beta \theta_w)^{1/3}$ and $L_s = \kappa^{2/3}/(g\beta\theta_w)^{1/3}$ are the intrinsic velocity and length scales. (*c*,*d*) Magnified view of the blue boxes in (*a*,*b*), respectively. The horizontal red line in (*a*) and (*c*) depicts the most energetic length scale $\lambda_z^+ = 600$ at $Gr_\delta = 1.1 \times 10^6$; the horizontal red line in (*b*) and (*d*) depicts the most energetic length scale $\lambda_z^+ = 130$ at $Gr_\delta = 2.7 \times 10^7$.

identification of this 'classical' regime is robust and the transition mechanism is consistent with the near-wall turbulence development discussed in § 3.2.

Previous literature suggests that the transition from the 'classical' turbulent regime to the ultimate regime results in a change of the heat transfer rate (e.g. Wells & Worster 2008; Grossmann & Lohse 2011; Ng *et al.* 2017). However, as discussed in §§ 3.1 and 3.2, the development of heat transfer and near-wall turbulence structure for the NCBL is gradual, and the transition from the weakly turbulent regime towards the highly turbulent regime is subtle (see also Ke *et al.* 2021). In the light of the unifying theory (e.g. Grossmann & Lohse 2000, 2011), the near-wall region of the weakly turbulent flow in the 'classical' regime would follow a laminar-like scaling (cf. Ng *et al.* 2015). Following the Prandtl–Blasius–Pohlhausen scaling (cf. Landau & Lifshitz 1987; Ng *et al.* 2015), one would expect the ratio of the wall-normal length scale (usually the boundary layer thickness) to the streamwise length scale (usually the downstream distance for spatially developing flows) to be a function of Reynolds number. However, for the present study, there is no natural length scale in the streamwise direction due to its parallel nature, therefore we adopt a length scale ratio between two wall-normal length scales:

$$\frac{\delta_u}{\delta_m} \equiv \frac{\rho \nu \bar{u}_m}{\delta_m \tau_w}. \tag{3.5}$$

Here, $\delta_u = \rho\nu\bar{u}_m/\tau_w$ approximates the thickness of the laminar boundary layer if the flow was laminar up to maximum velocity location δ_m. This length scale is also used by Ng *et al.* (2015) to distinguish the boundary-layer-like region from the bulk flow for natural convection in differentially heated channels. Equation (3.5) conveniently distinguishes the length scale development differences in different flow regimes, as shown in figure 9(*a*). To ease the comparison with non-buoyant flows, the bulk flow Reynolds number $Re_m = \delta_m\bar{u}_m/\nu$ is adopted as a measure of the flow development. In the laminar regime, the length scale ratio is given directly by the analytical expression

$$\frac{\delta_u}{\delta_m} = \frac{g\beta\theta_w\rho\nu\sqrt{\pi}\,\mathcal{V}}{\sqrt{Pr}\,(1-\sqrt{Pr})\,\eta_m} \approx 0.414, \tag{3.6}$$

where $\mathcal{V} = \mathrm{i}^2\mathrm{erfc}(\eta_m) - \mathrm{i}^2\mathrm{erfc}(\eta_m/\sqrt{Pr}) \approx 0.01731$ is a similarity constant at the (laminar) velocity maximum location $\eta_m \approx 0.39655$ (cf. Ke *et al.* 2019). The constant δ_u/δ_m in the laminar regime is expected since both δ_u and δ_m are wall-normal length scales and therefore follow the same scaling with the flow development. As seen in figure 9(*a*), our DNS show excellent agreement with (3.6) in the laminar regime until the flow undergoes laminar–turbulent transition, where δ_u/δ_m starts to decrease. Interestingly, as the flow enters the turbulent regime, a second constant δ_u/δ_m region emerges (for DNS-D this is $\delta_u/\delta_m \approx 0.25$) before it reduces again at higher Re_m (or, identically, Gr_δ). In the present study, we define the limits of this constant region as the Re_m at which the length scale ratio exceeds $\pm 10\,\%$ of the average value after the flow becomes turbulent, i.e. $|\delta_u/\delta_m - 0.25| \leq 0.025$ and $Gr_\delta > 10^6$ (cf. figure 2, where the Nusselt number starts to follow the empirical $1/3$ power law) for DNS-D (indicated by the horizontal grey shading in figure 9). With this criterion, the constant ratio region is identified at $290 < Re_m < 550$ for DNS-D, which corresponds to Grashof number range $10^6 < Gr_\delta < 5 \times 10^6$ (indicated by the vertical grey shading in figure 9). This result is consistent with the spanwise turbulence structure development shown in figure 7, where the energetic low-speed packets are seen reduced in strength at approximately $Gr_\delta \sim 10^6$; and the constant near-wall streak spacing that is commonly seen in fully turbulent flows starts to emerge for NCBL only at $Gr_\delta > 6.5 \times 10^6$. The existence of such a constant ratio region in the turbulent NCBL at relatively low Re_m (or Gr_δ) indicates that the near-wall structure of the turbulent flow in this regime may share characteristics and mechanisms similar to those of a laminar flow. Similar constant ratio regions are also seen in the measurements of Tsuji & Nagano (1988*a*) for the spatially developing NCBL with $\delta_u/\delta_m \approx 0.22$ at similar Re_m range, which implies that the measurements of Tsuji & Nagano (1988*a*) sit in this 'classical' weakly turbulent regime with a turbulent bulk flow and a laminar-like near-wall region, and in DNS-A with $\delta_u/\delta_m \approx 0.255$ at approximately $320 < Re_m < 700$ (corresponding to $2 \times 10^6 < Gr_\delta < 4 \times 10^6$). At higher Re_m (or Gr_δ), a further decrease is seen in figure 9(*a*) for DNS-D, which gradually approaches the numerical data in DNS-A and DNS-C with increasing Re_m, indicating that the flow becomes initial-condition-invariant. In this flow regime, the DNS data for DNS-C also agree well with the measurements of turbulent wall jet flows (Tachie *et al.* 2002; Naqavi *et al.* 2018), suggesting that at high enough Re_m, the near-wall region would become turbulent in the sense of von Kármán, and appear comparable with the canonical wall-bounded turbulence even though the two flows are driven differently – we will show in the following analysis that this is attributed to the development of the near-wall turbulence.

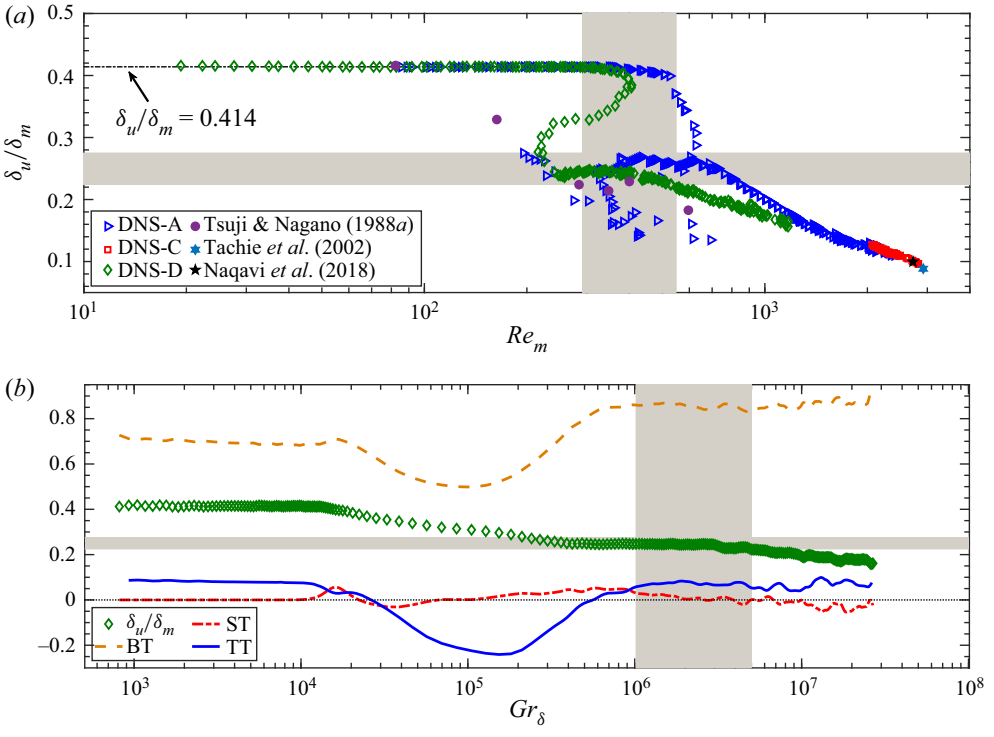

Figure 9. The length scale ratio development for the NCBL in (*a*) Reynolds number Re_m and (*b*) Grashof number Gr_δ, with individual contributions from (3.7) for DNS-D. The grey shaded areas indicate the range of the weakly turbulent regime for DNS-D in $290 < Re_m < 550$ (corresponding to $10^6 < Gr_\delta < 5 \times 10^6$) and the region $\delta_u/\delta_m = 0.25 \pm 0.025$. Open symbols represent the data of DNS-A (blue triangles), DNS-C (red squares) and DNS-D (green diamonds). Filled symbols denote data obtained from other sources: purple circles for experiment measurements of Tsuji & Nagano (1988*a*) for a spatially developing NCBL; navy hexagrams for experiment measurements of Tachie, Balachandar & Bergstrom (2002) for a wall jet; black stars for DNS data of Naqavi *et al.* (2018) for a wall jet. The horizontal black dotted line in (*b*) indicates the zero line.

To further investigate the near-wall characteristics in this constant-ratio region, the budget of the length scale ratio is obtained by taking the second integral of the mean streamwise momentum equation up to δ_m and normalised by a shear forcing $\delta_m \tau_w$, which reads

$$\frac{\delta_u}{\delta_m} = 1 + \underbrace{\frac{\rho}{\delta_m \tau_w} \int_0^{\delta_m} \int_0^y \frac{\partial \bar{u}}{\partial t} \,\mathrm{d}y \,\mathrm{d}y}_{\mathrm{TT}} - \underbrace{\frac{\rho}{\delta_m \tau_w} \int_0^{\delta_m} \int_0^y g\beta\bar{\theta} \,\mathrm{d}y \,\mathrm{d}y}_{\mathrm{BT}} + \underbrace{\frac{\rho}{\delta_m \tau_w} \int_0^{\delta_m} \overline{u'v'} \,\mathrm{d}y}_{\mathrm{ST}}, \tag{3.7}$$

where TT, BT and ST denote the temporal (unsteadiness), buoyancy and turbulent shear contributions to the length scale ratio. Ideally, for a steady laminar non-buoyant parallel flow with zero pressure gradient, terms BT, ST and TT are all zero, yielding $\delta_u = \delta_m$ as in the laminar Prandtl–Blasius–Pohlhausen scaling (Landau & Lifshitz 1987). For our NCBL flow, the individual contributions from these terms are depicted in figure 9(*b*). It is

clear that in the laminar regime, ST is zero while BT is mainly responsible for adjusting δ_u/δ_m. When the flow becomes turbulent, both TT and BT appear constant for the entire turbulent regime: TT shows a magnitude (TT ≈ 0.08) similar to its laminar value, while BT is elevated to BT ≈ 0.85 from the laminar state (BT ≈ 0.68). At relatively low Re_m in the turbulent regime, the turbulent shear term ST is close to zero (despite its initial decrease at $10^6 < Gr_\delta < 2 \times 10^6$ due to adjustment from the laminar–turbulent transition) – similar to that of ST in the laminar regime, resulting in a constant δ_u/δ_m in this regime – whereas at higher Re_m, ST becoming increasingly negative and therefore δ_u/δ_m attenuates in the highly turbulent regime. This suggests that the constant δ_u/δ_m region essentially refers to a turbulent flow regime where the near-wall momentum transfer due to turbulence is negligible (and therefore the 'weakly turbulent' or 'laminar-like' regime), while a further decrease in δ_u/δ_m at higher Re_m (or Gr_δ) is due mainly to the rising strength of the $\overline{u'v'}$ stress in the near-wall region (cf. figure 5*a*), which is also seen strongly in the canonical wall-bounded turbulence (e.g. channel flows and wall jets).

While the length scale ratio (3.5) describes the near-wall turbulence development, it is also directly linked to the skin friction coefficient C_f for the NCBL flow. By multiplying the bulk Reynolds number Re_m, (3.5) can be recast into

$$Re_m \frac{\delta_u}{\delta_m} = \frac{\rho \bar{u}_m^2}{\tau_w} = \frac{2}{C_f}. \tag{3.8}$$

From (3.8), a constant δ_u/δ_m that is seen in the laminar and weakly turbulent regimes would lead to $C_f \propto Re_m^{-1}$, as shown in figure 10, which is consistent with the skin friction correlation for Blasius boundary layers (with different prefactors). Note that the second equality of (3.8) can be rewritten as $C_f = 2/(u_m^+)^2$, such that the skin friction coefficient can also be approximated by the velocity log law (which starts to appear only at sufficiently high Re_m, or equivalently, Gr_δ) based on the maximum mean streamwise velocity u_m^+ in wall units. Although the formulation of the buoyancy-modified velocity log law (cf. Ke *et al.* 2020, equation (6.29)) relies on the buffer layer velocity u_c for which we have no model, in the present study we are able to apply the log-law approximation by fitting empirically u_c from DNS data. Despite the fact that the velocity maximum usually occurs beyond the extent of the log-law region, for high Re_m, flows the log-law approximation still demonstrates good agreement with the DNS data, as shown in figure 10. In this regime, the skin friction coefficient C_f also agrees well with a simplified approximation

$$C_f = \frac{2D^2}{\ln^2(0.06\,Re_m)}, \tag{3.9}$$

where $D = 0.31$ is a empirical prefactor associated with the mixing length coefficient (cf. the mixing length coefficient in the buoyancy modified log law in Ke *et al.* 2020) for our NCBL. This approximation (3.9) takes a similar form to the wall friction expression for the turbulent boundary layers (cf. Kestin & Persen 1962; White 1991; $C_f = 2D^2/\ln^2(0.06\,Re_x)$, with $D = 0.477$). With reference to figure 10, it further supports the idea that the turbulent NCBL has two distinct regimes: at relatively low Re_m, it follows $C_f \propto Re_m^{-1}$, representing a 'laminar-like' near-wall region, while at large Re_m, a log-law-type scaling is seen, which is indicative of a fully turbulent flow in the sense of von Kármán being developed.

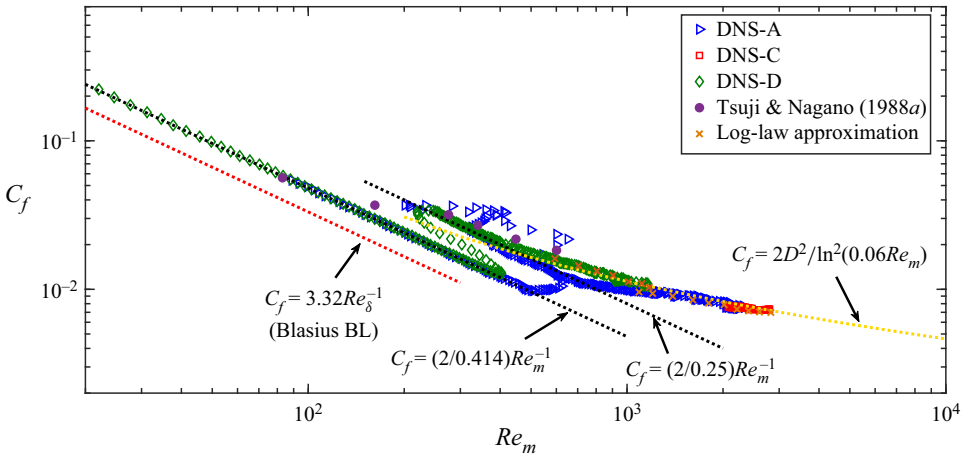

Figure 10. The skin friction coefficient C_f for the NCBL. The red dotted line indicates the skin friction coefficient for the laminar Blasius boundary layer (Reynolds number based on the disturbance thickness); black dotted lines correspond to the skin friction coefficient for the laminar regime $C_f = (2/0.414)\,Re_m^{-1}$ and the weakly turbulent regime $C_f = (2/0.25)\,Re_m^{-1}$ based on (3.8); orange crosses are the approximation of C_f by empirically fitting u_c to the log-law model (for clarity, not all data are shown); the yellow dotted line is indicative of the simplified approximation (3.9).

3.4. *Turbulence kinetic energy budget*

In this subsection, we explore how the turbulence in the near-wall region is produced and sustained by examining the turbulence kinetic energy budget. The energetic balance has been crucial in explaining the flow regimes and obtaining Nusselt number scaling relationships in canonical flows – for example, Rayleigh–Bénard flow (Grossmann & Lohse 2000, 2001, 2011) and differentially heated channel flow (Ng *et al.* 2018). Such information will lead to a better understanding of the turbulence mechanisms in the near-wall region, which may aid the development of scaling relationships for turbulence models.

For our temporally developing parallel flow ($\bar{v} = \partial\bar{\psi}/\partial x = \partial\bar{\psi}/\partial z = 0$, where ψ is an arbitrary flow variable of interest – note that for our temporally developing flow, the statistics are averaged spatially over the homogeneous x–z plane), the equation for the turbulence kinetic energy reads

$$\frac{\partial \bar{k}}{\partial t} = P + T_t + T_p + D_f + \varepsilon + \mathcal{B}, \tag{3.10}$$

where $\bar{k} = \overline{u_i'^2}/2$ is the turbulence kinetic energy, P represents the shear production, T_t is the turbulent convection, T_p is the pressure transport, D_f is the viscous diffusion, ε denotes the viscous dissipation, and $\mathcal{B}$ is the buoyancy flux term. The individual contributions from production, dissipation and transport terms towards the temporal evolution of the turbulence kinetic energy are given by

$$P = -\overline{u'v'}\,\frac{\partial \bar{u}}{\partial y}, \quad T_t = -\frac{\partial \overline{v'k}}{\partial y}, \quad T_p = -\frac{1}{\rho}\,\frac{\partial \overline{v'p'}}{\partial y}, \tag{3.11a,b,c}$$

$$D_f = \nu\,\frac{\partial^2 \bar{k}}{\partial y^2}, \quad \varepsilon = -\nu\,\overline{\left(\frac{\partial u_i'}{\partial x_j}\right)^2}, \quad \mathcal{B} = g\beta\,\overline{u'\theta'}. \tag{3.11d,e,f}$$

Figure 11 shows the contributors in (3.11) to the turbulence kinetic energy in the 'classical' regime (figure 11*a*) and the fully turbulent ultimate regime (figures 11*b*–figure 11*a*). As shown in figure 11(*a*), there exist two local peaks for the shear production P. Such a structure is typical in flows with two shear layers under similar general flow geometries (e.g. the planar wall jet flows; Naqavi *et al.* 2018; Gnanamanickam *et al.* 2019) as these are the signature of the energetic mixing in the shear layers. For our NCBL flow, the shear production P has an inner local peak at $y^+ \approx 10$, which corresponds to the near-wall shear layer as would have been seen in the canonical boundary layer flows, and an outer peak at $y/\delta_m \approx 4$, which corresponds to the free shear layer in the bulk flow. Although the near-wall turbulent shear $\overline{u'v'}$ is negligible in the 'classical' regime (see figure 5*a*), as seen in figure 11(*a*), the inner peak of the shear production still shows a similar magnitude to the outer peak. However, the buoyancy flux term is shown to have only minimal effect (with slightly negative values) in this region – the primary role of buoyancy is to accelerate the mean flow (see Ke *et al.* 2020), which generates turbulence via shear production, rather than direct buoyant production of turbulence. It can be seen that in addition to the shear production, the near-wall turbulence at this stage is transported predominantly from the outer bulk flow by pressure T_p. The net gain of the turbulence kinetic energy is balanced by the viscous dissipation (and diffusion for $y^+ > 5$), while turbulent transport is rather weak since the near-wall flow is laminar-like with small turbulent fluctuation intensity. Away from the wall, the buoyancy flux term contributes positively to the turbulence generation in the bulk flow over a large distance ($0.2 < y/\delta_m < 10$ for DNS-D at $Gr_\delta = 1.1 \times 10^6$ with peak $\mathcal{B}\nu/u_\tau^4 \approx 0.01$) due to the excursion of warmer fluid parcels from the near-wall region (recall in figure 5(*a*), $\overline{u'v'}$ is positive in the bulk flow region). In the free shear layer ($y/\delta_m > 1$), shear production P, being the dominant term driving turbulence, is balanced mainly by dissipation – with the excess energy being transported towards the edge of the flow as well as the maximum velocity location. This suggests that the outer bulk flow has indirect influence on the near-wall region by adjusting the energetic behaviour at $y \sim \delta_m$. Similar transport effects on the near-wall turbulence are also seen in planar wall jets (Naqavi *et al.* 2018), where turbulence in the low-production region (which is also identified as the interaction zone of two shear layers) is typically maintained by a high level of turbulent transportation.

At higher Gr_δ, the flow enters the fully turbulent regime as shown in figure 11(*b*); the near-wall shear production grows in strength and becomes dominant in this region (at $Gr_\delta = 2.7 \times 10^7$ it is approximately four times larger than the outer peak); and the buoyancy flux term remains negligible in the near-wall region and shrinks in magnitude (with peak $\mathcal{B}\nu/u_\tau^4 \approx 0.004$) in the outer bulk flow. While both turbulent and pressure transport terms are following behaviour similar to the weakly turbulent case in figure 11(*a*), it gives a higher level of turbulent transport and a lower level of pressure transport in the near-wall region as the flow becomes more turbulent. Figure 11(*c*) shows a magnified view of these contributors at $Gr_\delta = 2.7 \times 10^7$ in the near-wall region, and compares with the DNS data taken from Kasagi & Nishimura (1997) for a combined convection in a differentially heated channel with aiding ambient flow at $Re_\tau = 86$ (based on δ_m). It can be seen that despite the close Re_τ reported, the data of Kasagi & Nishimura (1997) show a higher level of production, dissipation and turbulent transport, and a lower level of pressure effect in the vicinity of the wall ($y^+ < 60$) than our DNS-D at $Re_\tau \approx 85$. Such a discrepancy is not surprising as the combined convection has a more energetic flow in the near-wall region with the aid of ambient momentum (cf. Kasagi & Nishimura (1997) for the near-wall shear stress), resulting a higher level of shear and a more turbulent flow in

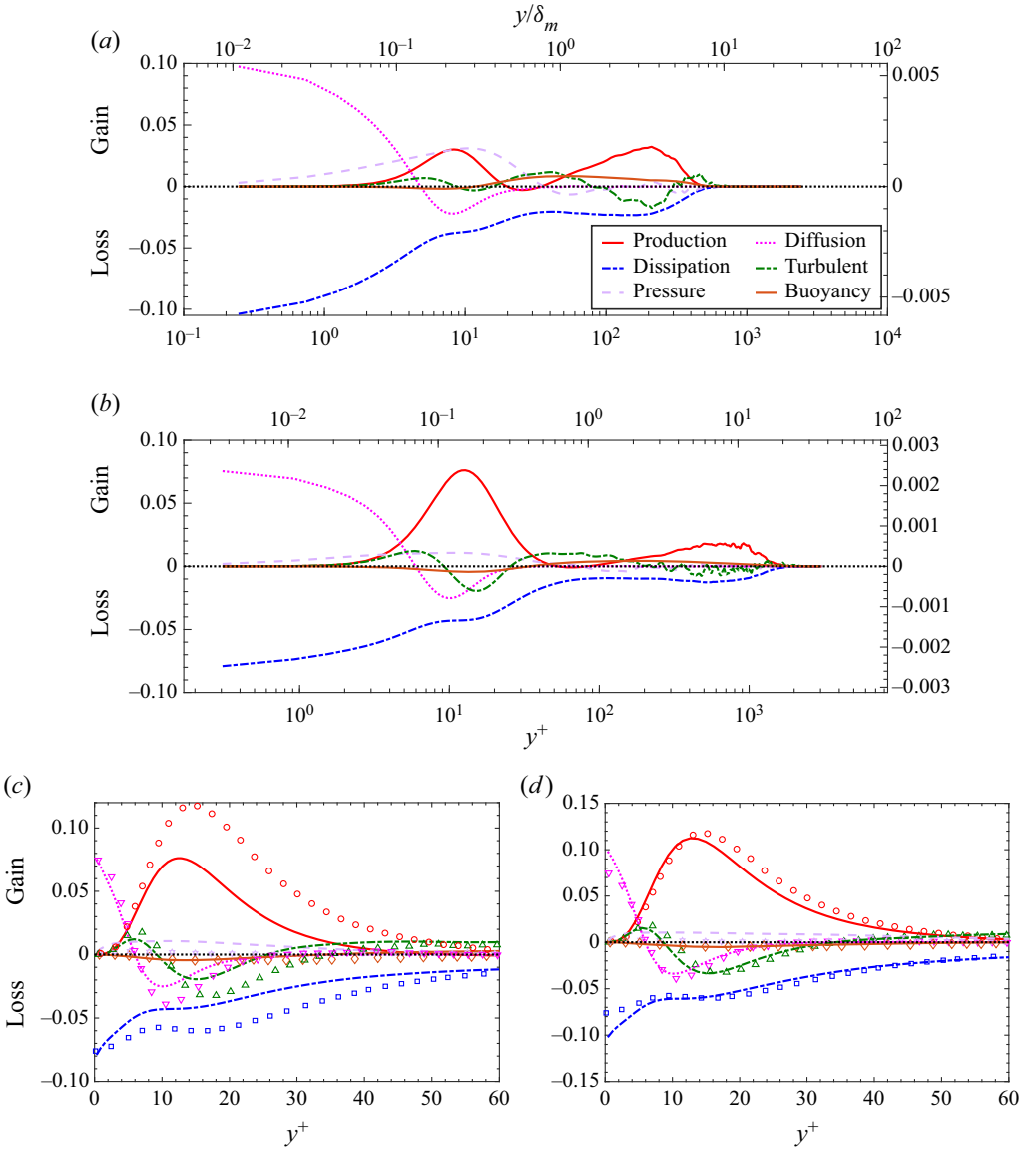

Figure 11. The turbulence kinetic energy budget of the temporally developing NCBL at (*a*) DNS-D, $Gr_\delta = 1.1 \times 10^6$ ($Re_\tau \approx 34$), and (*b*) DNS-D, $Gr_\delta = 2.7 \times 10^7$ ($Re_\tau \approx 85$). (*c*) Magnified view of the data shown in (*b*) in the near-wall region. (*d*) The near-wall region of DNS-A at $Gr_\delta = 4.1 \times 10^7$ ($Re_\tau \approx 117$). All terms are normalised into wall units with $\bar{u}_m^3/\delta_m$ (left-hand axis) and u_τ^4/ν (right-hand axis) in (*a*,*b*), while data in (*c*,*d*) are shown in wall units. Lines denote the DNS results from DNS-A and DNS-D; symbols in (*c*,*d*) denote the DNS data in wall coordinate taken from Kasagi & Nishimura (1997) for a combined convection in a differentially heated channel with aiding ambient flow at $Re_\tau = 86$. Colours represent individual components of the turbulence kinetic energy budget: red for shear production; blue for viscous dissipation; magenta for viscous diffusion; green for turbulent convection; lilac for pressure transport; orange for buoyancy production. Black dotted lines mark the zero line.

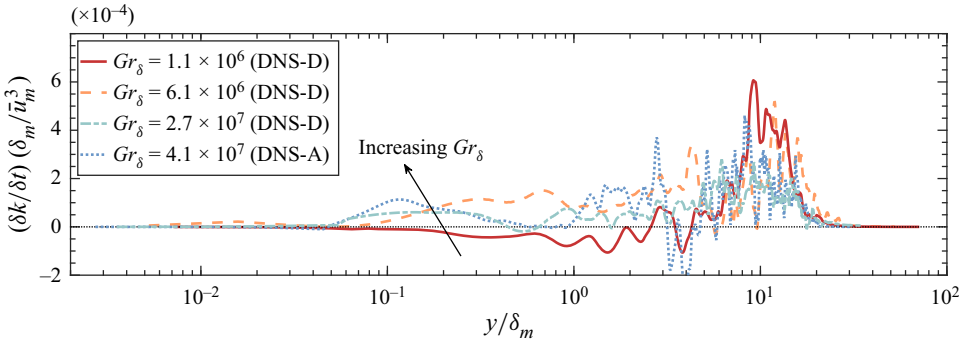

Figure 12. The temporal evolution of the turbulence kinetic energy (normalised with the outer bulk scales δ_m and $\bar{u}_m$) for the NCBL at different Grashof numbers. The horizontal dotted line indicates $\partial k/\partial t = 0$.

the near-wall region. This is supported by the fact that their data appear more comparable to our temporal NCBL at a much higher Grashof number: as shown in figure 11(*d*), our DNS-A at $Re_\tau \approx 117$ ($Gr_\delta = 4.1 \times 10^7$ in the fully turbulent regime) demonstrates relatively good quantitative agreement with the combined convection at $Re_\tau = 86$ (again we note that Re_τ alone does not fully characterise the NCBL flow since the buoyancy effects are not accounted for).

The sum of the right-hand-side terms in (3.11), giving the temporal growth of the turbulence kinetic energy, is shown in figure 12. We note that this temporal evolution rate is more than an order of magnitude smaller than the contributors shown in figure 11. Despite the strong oscillations due to the small magnitude and the temporal nature of the turbulence flow, figure 12 still shows a clear signature of the turbulence energy evolution for the NCBL: for all data shown, the temporal growth of turbulence occurs predominantly in the outer bulk flow (i.e. the free shear layer) with a distributed peak at $y/\delta_m \approx 10$. At $Gr_\delta = 1.1 \times 10^6$, the turbulence energy experiences a weak decay (negative growth rate) in the near-wall region $y/\delta_m < O(1)$. With increasing Grashof number, owing to a growing local production at $y/\delta_m \approx 0.1$ (cf. figure 11*b*), the turbulence growth rate attains a positive value and spreads to a wider area towards the near-wall region, giving rise to a net local turbulence energy gain in the near-wall region.

Figure 13 shows the production–dissipation equilibrium for the temporally developing NCBL flow in wall coordinate (figure 13*a*) and the outer bulk scale δ_m (figure 13*b*). Also shown in figure 13 are the DNS results of a combined convection at $Re_\tau = 86$ (Kasagi & Nishimura 1997), a turbulent channel flow at $Re_\tau = 180$ (Moser *et al.* 1999; Re_τ based on the channel half-width), and a planar wall jet at $Re_\tau = 210$ (Gnanamanickam *et al.* 2019; Re_τ based on δ_m). This ratio of shear production to viscous dissipation P/ε evaluates the balance between local production and destruction of the turbulent energy, and is a key parameter that characterises the logarithmic layer for canonical wall-bounded forced flows. In the near-wall region, as depicted in figure 13(*a*), P/ε increases with increasing Gr_δ since the shear becomes progressively stronger with the development of the flow: at $Gr_\delta = 1.1 \times 10^6$, dissipation exceeds production, $P/\varepsilon < 1$, suggesting that the near-wall turbulence is sustained with the transportation of energy from regions away from the wall; at higher Gr_δ, production exceeds dissipation, and the P/ε profile is more comparable to the forced flows reported by Kasagi & Nishimura (1997) and Moser *et al.* (1999) for $y^+ < 30$. Beyond $y^+ = 30$, the production and dissipation are almost in balance (such that $P/\varepsilon \approx 1$) for the channel flow in the log-law region ($30 < y+ < O(10^2)$),

whereas such a plateau is absent for our NCBL. The balanced production and dissipation (i.e. $P/\varepsilon \approx 1$) is often observed in the logarithmic layer for the canonical forced wall-bounded flows, and it has been seen as a prerequisite to obtain a valid mixing length model for the log-law region (Pope 2001). For our vertical NCBL flow, it is shown in figure 13 that the production–dissipation ratio P/ε follows a fundamentally different profile in the log-law region – despite the absence of the canonical P/ε prerequisite for the log-law, the NCBL flow can still be very well modelled by the mixing length model with a buoyancy-adjusted log-law (cf. Ke *et al.* 2020). Similar P/ε behaviour in this region is also seen in the combined convection in a differentially heated channel (Kasagi & Nishimura 1997) and the planar wall jet (Gnanamanickam *et al.* 2019), which is suggestive that the missing equilibrium here might due to the interaction of shear layers since the production is forced to zero at $y = \delta_m$ with $\partial\bar{u}/\partial y = 0$. In the region $0.6 < y/\delta_m < 1$ (see figure 13*b*), P/ε of our NCBL flow decays quickly to its minimum, which is slightly negative. The lack of production suggests a high level of transport from the neighbouring shear layers in order to preserve turbulence in this region (cf. figure 11, high level of turbulent transport in this region). This is consistent with the observation of the planar wall jet flows that P/ε is either very small or negative in the interaction zone (Irwin 1973; Zhou, Heine & Wygnanski 1996; Dejoan & Leschziner 2005). This interaction zone for our temporally developing NCBL is seen to decline in size with increasing Gr_δ. Farther away in the bulk region ($y/\delta_m > 1$, see figure 13*b*), a high level of production is observed for our NCBL flow. In this region, the shear production is typically associated with the temporal growth of the boundary layer thickness due to entrainment (cf. Ke *et al.* 2021; the entrainment coefficient is dominated by the total shear production in the bulk region). Meanwhile, the production–dissipation ratio is approximately constant at $P/\varepsilon \approx 1.5$ regardless of Gr_δ, while for the planar wall jet (Gnanamanickam *et al.* 2019), the production is in equilibrium with the dissipation, giving a unity P/ε in the free shear layer. This value is close to that of the homogeneous shear flows with uniform mean velocity gradient (e.g. Tavoularis & Corrsin 1981; Rogers & Moin 1987; De Souza, Nguyen & Tavoularis 1995; giving $P/\varepsilon \approx 1.4 \sim 1.7$) in which the transport process is absent and the excess energy completely contributes to the exponential growth of the turbulence in time. However, in our temporally developing NCBL, the excessive energy generated by shear is mostly transported towards the interaction zone by turbulent transport (cf. figure 11, T_t is about half of ε), which implicitly affects the near-wall turbulence by adjusting the turbulence balance in this low-production region, while the remainder contributes to the temporal growth of the turbulence.

4. Conclusions

In this paper, a vertical natural convection boundary layer (NCBL) with $Pr = 0.71$ has been investigated using direct numerical simulations (DNS) in a temporal framework. Previous studies have suggested that there is a change in the heat transfer rate for turbulent NCBLs from a 'classical' $1/3$ power law to a higher ultimate heat transfer (Grossmann & Lohse 2000; Ng *et al.* 2017) at large Grashof number. While such a transition in the turbulent heat transfer is expected, this process has been shown to develop very slowly and subtly over a very large range of Grashof number (Wells & Worster 2008; Ng *et al.* 2017; Ke *et al.* 2021), and as such, it is difficult to discern the regime change in the turbulence development. In the present study, clear evidence is presented showing the presence of a regime where the outer bulk flow is turbulent but in which the near-wall region is predominantly laminar, consistent with the development for canonical wall-bounded turbulence (Kraichnan 1962; Grossmann & Lohse 2000).

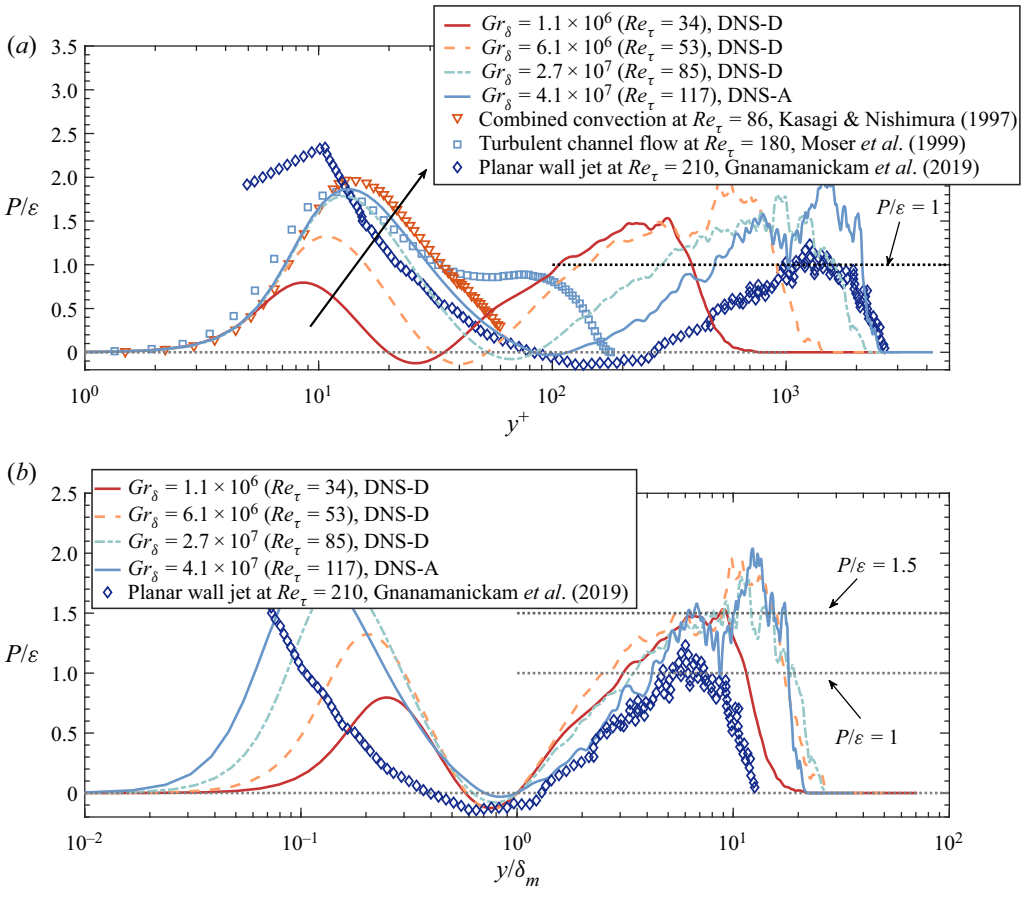

Figure 13. Production–dissipation ratio in the near-wall region (*a*) in wall coordinate and (*b*) normalised by the bulk flow length scale δ_m. The arrow in (*a*) shows the direction of increasing Gr_δ for cases with buoyancy. Horizontal dotted lines in (*a*,*b*) indicate $P/\varepsilon = 0$, 1 and 1.5.

Turbulent statistics, momentum balance and the development of energy spectra support this conclusion. We show that the Reynolds shear stress has a close-to-zero negative trough in the near-wall region after laminar–turbulent transition since the near-wall momentum transfer due to turbulence mixing is weak in the 'classical' regime, which is consistent with the existing measurements (Tsuji & Nagano 1988*a*; Abedin *et al.* 2009; Nakao *et al.* 2017). With increasing Grashof number, the negative trough becomes larger in magnitude as the turbulent momentum transfer grows in strength. A similar trend has been seen strongly in canonical wall-bounded turbulence (e.g. Moser *et al.* 1999) and buoyancy-driven channel flows (e.g. Kim *et al.* 2021). Further evidence may be seen in the streamwise turbulence intensity development, where it develops gradually from a mono-peak profile into a dual-peak structure. Using premultiplied power spectra of the streamwise velocity fluctuation, we show that the growing inner peak of the $\overline{u'u'}$ stress is located at a fixed location and wavelength ($y^+ = 18$ and $\lambda_x^+ = 1000$) in the viscous coordinate, similar to that in canonical wall-bounded turbulence (Del Alamo *et al.* 2004; Hutchins & Marusic 2007*b*). In contrast to the forced flows where the outer energetic peak, which accounts for the logarithmic region for these flows, becomes visible only at sufficiently high Reynolds

number and after the inner peak has been developed, the emerging inner peak in our DNS data suggests that the NCBL follows a different turbulence development. Further evidence is also seen in the spanwise premultiplied spectra, which are representative of the near-wall streak spacing in the fully turbulent regime. It is shown that the mean streak spacing varies appreciably with Gr_δ at relatively low Grashof number ($10^6 < Gr_\delta < 6.5 \times 10^6$; in this regime, the NCBL is generally thought turbulent in the literature), while at higher Gr_δ, it is approximately constant, $\lambda_z^+ \approx 130$. Such a constant spacing marks the formation of the turbulent near-wall streaks that is commonly seen in fully turbulent wall-bounded flows (Kline *et al.* 1967; Klewicki *et al.* 1995; Tomkins & Adrian 2003; Patel *et al.* 2016), which is suggestive of a second stage of the turbulence development.

Following the Prandtl–Blasius–Pohlhausen scaling (Landau & Lifshitz 1987; Ng *et al.* 2015), we identified the weakly turbulent 'classical' regime in which the length scale ratio δ_u/δ_m is a constant. By comparing our DNS with previous datasets, this 'classical' regime is found to span approximately $250 < Re_m < 550$ for both DNS-D and the measurements of Tsuji & Nagano (1988*a*). This Reynolds number range is equivalent to $10^6 < Gr_\delta < 5 \times 10^6$ for DNS-D, which appears consistent with the development of the near-wall streaks. On further analysis, we show that such a constant δ_u/δ_m is indeed attributed to a negligible near-wall turbulence in this Reynolds number range. In this regime, the skin friction coefficient C_f is shown to follow a laminar-like scaling with the bulk Reynolds number. At higher Re_m (or Gr_δ), a log-law-type scaling is seen for C_f, which further supports that the near-wall region has been developed into a fully turbulent one.

To provide a more complete view of the near-wall turbulence generation and development, we further investigated the energetic contributors to the turbulence kinetic energy balance. For the NCBL, there exist two local peaks for the shear production, corresponding to the two shear layers in the flow. At $Gr_\delta = 1.1 \times 10^6$, the near-wall peak of the shear production has magnitude similar to its outer counterpart, and the turbulent transport is small since the flow is weakly turbulent in the 'classical' regime. The near-wall turbulence at this stage is sustained predominantly by the pressure transport in addition to the shear production. With increasing Gr_δ, the flow enters the fully turbulent regime, and both turbulent transport and shear production grow in magnitude while the pressure transport gradually loses its significance. We show that the buoyancy flux term is negligibly small in the near-wall region with negative values, while it contributes positively to the turbulence generation in the bulk flow. These results suggest that the NCBL develops in a way such that the near-wall turbulence is driven by the turbulent outer bulk until it is sufficiently large that turbulence can be generated and sustained locally. Upon further investigation, we show that the production–dissipation balance of our NCBL follows a fundamentally different profile to that of the canonical wall-bounded turbulence where an equilibrium $P/\varepsilon = 1$ is expected in the log-law region, and such a discrepancy may be attributed to the interaction between the shear layers. While P/ε grows in magnitude with increasing Gr_δ in the near-wall region, it remains at an approximately constant value across the outer bulk flow, with $P/\varepsilon \approx 1.5$ regardless of Gr_δ. The excessive energy in the bulk region is transported to the velocity maximum location (the low-production region where the two shear layers interact) by turbulent transport and therefore affects the near-wall turbulence generation.

These results have implications for a better understanding of the near-wall turbulence mechanisms for NCBL flows, which may aid the development of scaling relationships for turbulence models.

Acknowledgements. The authors gratefully acknowledge the computational resources provided by the Institute of Fluid Science, Tohoku University, and by the Sydney Informatics Hub, University of Sydney.

Declaration of interests. The authors report no conflict of interest.

Author ORCIDs.
Junhao Ke https://orcid.org/0000-0002-1177-1834;
N. Williamson https://orcid.org/0000-0001-7246-8356;
S.W. Armfield https://orcid.org/0000-0002-8032-0017;
A. Komiya https://orcid.org/0000-0002-1645-6040.

References

Abedin, M.Z., Tsuji, T. & Hattori, Y. 2009 Direct numerical simulation for a time-developing natural-convection boundary layer along a vertical flat plate. *Intl J. Heat Mass Transfer* **52** (19–20), 4525–4534.

Antonia, R.A., Teitel, M., Kim, J. & Browne, L.W.B. 1992 Low-Reynolds-number effects in a fully developed turbulent channel flow. *J. Fluid Mech.* **236**, 579–605.

Bayley, F.J. 1955 An analysis of turbulent free-convection heat-transfer. *Proc. Inst. Mech. Engrs* **169** (1), 361–370.

Cheesewright, R. 1968 Turbulent natural convection from a vertical plane surface. *Trans. ASME J. Heat Transfer* **90** (1), 1–6.

Cooper, P. & Hunt, G.R. 2010 The ventilated filling box containing a vertically distributed source of buoyancy. *J. Fluid Mech.* **646**, 39–58.

De Souza, F.A., Nguyen, V.D. & Tavoularis, S. 1995 The structure of highly sheared turbulence. *J. Fluid Mech.* **303**, 155–167.

Dejoan, A. & Leschziner, M.A. 2005 Large eddy simulation of a plane turbulent wall jet. *Phys. Fluids* **17** (2), 025102.

Del Alamo, J.C., Jiménez, J., Zandonade, P. & Moser, R.D. 2004 Scaling of the energy spectra of turbulent channels. *J. Fluid Mech.* **500**, 135–144.

George, W.K. & Capp, S.P. 1979 A theory for natural convection turbulent boundary layers next to heated vertical surfaces. *Intl J. Heat Mass Transfer* **22** (6), 813–826.

Gnanamanickam, E.P., Bhatt, S., Artham, S. & Zhang, Z. 2019 Large-scale motions in a plane wall jet. *J. Fluid Mech.* **877**, 239–281.

Grossmann, S. & Lohse, D. 2000 Scaling in thermal convection: a unifying theory. *J. Fluid Mech.* **407**, 27–56.

Grossmann, S. & Lohse, D. 2001 Thermal convection for large Prandtl numbers. *Phys. Rev. Lett.* **86** (15), 3316.

Grossmann, S. & Lohse, D. 2011 Multiple scaling in the ultimate regime of thermal convection. *Phys. Fluids* **23** (4), 045108.

Hölling, M. & Herwig, H. 2005 Asymptotic analysis of the near-wall region of turbulent natural convection flows. *J. Fluid Mech.* **541**, 383–397.

Howland, C.J., Ng, C.S., Verzicco, R. & Lohse, D. 2022 Boundary layers in turbulent vertical convection at high Prandtl number. *J. Fluid Mech.* **930**, A32.

Hutchins, N. & Marusic, I. 2007*a* Evidence of very long meandering features in the logarithmic region of turbulent boundary layers. *J. Fluid Mech.* **579**, 1–28.

Hutchins, N. & Marusic, I. 2007*b* Large-scale influences in near-wall turbulence. *Phil. Trans. R. Soc.* A **365** (1852), 647–664.

Illingworth, C.R. 1950 Unsteady laminar flow of gas near an infinite flat plate. In *Mathematical Proceedings of the Cambridge Philosophical Society*, vol. 46, pp. 603–613. Cambridge University Press.

Irwin, H.P.A.H. 1973 Measurements in a self-preserving plane wall jet in a positive pressure gradient. *J. Fluid Mech.* **61** (1), 33–63.

Kasagi, N. & Nishimura, M. 1997 Direct numerical simulation of combined forced and natural turbulent convection in a vertical plane channel. *Intl J. Heat Fluid Flow* **18** (1), 88–99.

Ke, J., Williamson, N., Armfield, S.W., Komiya, A. & Norris, S.E. 2021 High Grashof number turbulent natural convection on an infinite vertical wall. *J. Fluid Mech.* **929**, A15.

Ke, J., Williamson, N., Armfield, S.W., McBain, G.D. & Norris, S.E. 2019 Stability of a temporally evolving natural convection boundary layer on an isothermal wall. *J. Fluid Mech.* **877**, 1163–1185.

KE, J., WILLIAMSON, N., ARMFIELD, S.W., NORRIS, S.E. & KOMIYA, A. 2020 Law of the wall for a temporally evolving vertical natural convection boundary layer. *J. Fluid Mech.* **902**, A31.

KESTIN, J. & PERSEN, L.N. 1962 Application of Schmidt's method to the calculation of Spalding's function and of the skin-friction coefficient in turbulent flow. *Intl J. Heat Mass Transfer* **5** (3–4), 143–152.

KIM, K.-H., AHN, J. & CHOI, J.-I. 2021 Mean thermal energy balance analysis in differentially heated vertical channel flows. *Phys. Fluids* **33** (6), 065120.

KLEWICKI, J.C., METZGER, M.M., KELNER, E. & THURLOW, E.M. 1995 Viscous sublayer flow visualizations at $Re_\theta = 1\,500\,000$. *Phys. Fluids* **7** (4), 857–863.

KLINE, S.J., REYNOLDS, W.C., SCHRAUB, F.A. & RUNSTADLER, P.W. 1967 The structure of turbulent boundary layers. *J. Fluid Mech.* **30** (4), 741–773.

KRAICHNAN, R.H. 1962 Turbulent thermal convection at arbitrary Prandtl number. *Phys. Fluids* **5** (11), 1374–1389.

LANDAU, L. & LIFSHITZ, E. 1987 *Fluid Mechanics*. Pergamon.

MACDONALD, M., CHUNG, D., HUTCHINS, N., CHAN, L., OOI, A. & GARCÍA-MAYORAL, R. 2017 The minimal-span channel for rough-wall turbulent flows. *J. Fluid Mech.* **816**, 5–42.

MARUSIC, I., UDDIN, A.K.M. & PERRY, A.E. 1997 Similarity law for the streamwise turbulence intensity in zero-pressure-gradient turbulent boundary layers. *Phys. Fluids* **9** (12), 3718–3726.

MATHIS, R., HUTCHINS, N. & MARUSIC, I. 2009 Large-scale amplitude modulation of the small-scale structures in turbulent boundary layers. *J. Fluid Mech.* **628**, 311–337.

MORTON, B.R., TAYLOR, G.I. & TURNER, J.S. 1956 Turbulent gravitational convection from maintained and instantaneous sources. *Proc. R. Soc. Lond.* A **234** (1196), 1–23.

MOSER, R.D., KIM, J. & MANSOUR, N.N. 1999 Direct numerical simulation of turbulent channel flow up to $Re_\tau = 590$. *Phys. Fluids* **11** (4), 943–945.

NAKAO, K., HATTORI, Y. & SUTO, H. 2017 Numerical investigation of a spatially developing turbulent natural convection boundary layer along a vertical heated plate. *Intl J. Heat Fluid Flow* **63**, 128–138.

NAQAVI, I., TYACKE, J. & TUCKER, P. 2018 Direct numerical simulation of a wall jet: flow physics. *J. Fluid Mech.* **852**, 507–542.

NG, C.S., OOI, A., LOHSE, D. & CHUNG, D. 2015 Vertical natural convection: application of the unifying theory of thermal convection. *J. Fluid Mech.* **764**, 349–361.

NG, C.S., OOI, A., LOHSE, D. & CHUNG, D. 2017 Changes in the boundary-layer structure at the edge of the ultimate regime in vertical natural convection. *J. Fluid Mech.* **825**, 550–572.

NG, C.S., OOI, A., LOHSE, D. & CHUNG, D. 2018 Bulk scaling in wall-bounded and homogeneous vertical natural convection. *J. Fluid. Mech.* **841**, 825–850.

ORTIZ, A.V., KOLOSZAR, L. & PLANQUART, P. 2019 Large eddy simulations on a natural convection boundary layer at $Pr = 0.71$ and 0.025. *Nucl. Engng Des.* **353**, 110231.

PATEL, A., BOERSMA, B.J. & PECNIK, R. 2016 The influence of near-wall density and viscosity gradients on turbulence in channel flows. *J. Fluid Mech.* **809**, 793–820.

POPE, S.B. 2001 *Turbulent Flows*. IOP.

ROGERS, M.M. & MOIN, P. 1987 The structure of the vorticity field in homogeneous turbulent flows. *J. Fluid Mech.* **176**, 33–66.

SAUNDERS, O.A. 1936 The effect of pressure upon natural convection in air. Proc. R. Soc. Lond. *A* **157** (891), 278–291.

SAUNDERS, O.A. 1939 Natural convection in liquids. *Proc. R. Soc. Lond.* A **172** (948), 55–71.

SCHETZ, J.A. & EICHHORN, R. 1962 Unsteady natural convection in the vicinity of a doubly infinite vertical plate. *J. Heat Transfer* **84** (4), 334–338.

SHIRI, A. & GEORGE, W.K. 2008 Turbulent natural convection in a differentially heated vertical channel. In *ASME 2008 Heat Transfer Summer Conference Collocated with the Fluids Engineering, Energy Sustainability, and 3rd Energy Nanotechnology Conferences, Jacksonville, FL*, pp. 285–291. American Society of Mechanical Engineers Digital Collection.

SIEBERS, D.L., MOFFATT, R.F. & SCHWIND, R.G. 1985 Experimental, variable properties natural convection from a large, vertical, flat surface. *J. Heat Transfer* **107** (1), 124–132.

SMITH, C.R. & METZLER, S.P. 1983 The characteristics of low-speed streaks in the near-wall region of a turbulent boundary layer. *J. Fluid Mech.* **129**, 27–54.

TACHIE, M., BALACHANDAR, R. & BERGSTROM, D. 2002 Scaling the inner region of turbulent plane wall jets. *Exp. Fluids* **33** (2), 351–354.

TAVOULARIS, S. & CORRSIN, S. 1981 Experiments in nearly homogeneous turbulent shear flow with a uniform mean temperature gradient. Part 1. *J. Fluid Mech.* **104**, 311–347.

TOMKINS, C.D. & ADRIAN, R.J. 2003 Spanwise structure and scale growth in turbulent boundary layers. *J. Fluid Mech.* **490**, 37–74.

TSUJI, T. & NAGANO, Y. 1988*a* Characteristics of a turbulent natural convection boundary layer along a vertical flat plate. *Intl J. Heat Mass Transfer* **31** (8), 1723–1734.

TSUJI, T. & NAGANO, Y. 1988*b* Turbulence measurements in a natural convection boundary layer along a vertical flat plate. *Intl J. Heat Mass Transfer* **31** (10), 2101–2111.

TSUJI, T. & NAGANO, Y. 1989 Velocity and temperature measurements in a natural convection boundary layer along a vertical flat plate. *Exp. Therm. Fluid Sci.* **2** (2), 208–215.

WARNER, C.Y. & ARPACI, V.S. 1968 An experimental investigation of turbulent natural convection in air at low pressure along a vertical heated flat plate. *Intl J. Heat Mass Transfer* **11** (3), 397–406.

WEI, T., WANG, Y. & ABRAHAM, J. 2021*a* Integral properties of turbulent natural convection over a vertical flat plate. *Intl Commun. Heat Mass Transfer* **125**, 105286.

WEI, T., WANG, Y. & ABRAHAM, J. 2021*b* Layered structure of turbulent natural convection over a vertical flat plate. *Intl J. Heat Mass Transfer* **181**, 121866.

WEI, T. & WILLMARTH, W.W. 1989 Reynolds-number effects on the structure of a turbulent channel flow. *J. Fluid Mech.* **204**, 57–95.

WELLS, A.J. & WORSTER, M.G. 2008 A geophysical-scale model of vertical natural convection boundary layers. *J. Fluid Mech.* **609**, 111–137.

WHITE, F.M. 1991 *Viscous Fluid Flow*. McGraw-Hill.

WILLIAMSON, N., ARMFIELD, S.W., KIRKPATRICK, M.P. & NORRIS, S.E. 2015 Transition to stably stratified states in open channel flow with radiative surface heating. *J. Fluid Mech.* **766**, 528–555.

ZHOU, M.D., HEINE, C. & WYGNANSKI, I. 1996 The effects of excitation on the coherent and random motion in a plane wall jet. *J. Fluid Mech.* **310**, 1–37.